Structure formation in a two-layer liquid polymer system

Dissertation

zur Erlangung des Grades
des Doktors der Naturwissenschaften
der Naturwissenschaftlich-Technischen Fakultät
der Universität des Saarlandes

Von

Roghayeh Shiri

Saarbrücken
2021

Tag des Kolloquiums:	July 26th, 2021
Dekan:	Prof. Dr. Jörn Walter
Berichterstatter:	Prof. Dr. Ralf Seemann
	Prof. Dr. Roland Bennewitz
Vorsitz:	Prof. Dr. Christian Motz
Akad. Mitarbeiter:	Dr. Hendrik Häll

Abstract

The instability of a thin liquid polystyrene (PS) film on a liquid polymethyl-methacrylate (PMMA) substrate is investigated and the evolution of the interfaces is monitored in situ by Atomic Force Microscopy (AFM) on the PS-air and by ex situ AFM studies on the PS-PMMA interface after removing the PS top layer by a selective solvent. In such a system, for film thicknesses in the range of inter molecular forces, the upper PS film is destabilized by long range Van der Waals forces leading to spinodal dewetting of the PS film.

To characterize the spinodal dewetting, we provide experimental measurements on the preferred wavelength and rupture time for different thickness of PS film. In contrast to the dewetting of liquid from a solid substrate, the buried interface is also able to deform and the PS-air and PS-PMMA interfaces develop in a coupled way. The amplitude of the spinodal corrugations on the interfaces is correlated with the respective interfacial energy and thus the amplitude of the buried PS-PMMA interface is substantially larger than that of the free PS-air interface. Despite the smaller driving forces compared with PS film on SiO_2, the characteristic wavelength is smaller for PS films on PMMA substrate. Surprisingly, it was found that the initial roughness of both interfaces can influence the mode selection process that explains the small deviation from the experimental results to theoretical modeling based on linear stability analysis.

Kurzzusammenfassung

Die Instabilität eines dünnen flüssigen Polystyrol (PS)-Films auf einem flüssigen Polymethyl-Methacrylat (PMMA)-Substrat wird untersucht und die Entwicklung der Grenzflächen in situ durch Rasterkraftmikroskopie (AFM) an der PS-Luft und durch ex situ AFM-Studien an der PS-PMMA-Grenzfläche nach Entfernung der PS-Oberschicht durch ein selektives Lösungsmittel verfolgt. In einem solchen System wird bei Schichtdicken im Bereich der intermolekularen Kräfte der obere PS-Film durch langreichweitige Van-der-Waals-Kräfte destabilisiert, was zu einer spinodalen Entnetzung des PS-Films führt.

Um die spinodale Entnetzung zu charakterisieren, bestimment wir in experimentellen Messungen die bevorzugte (spinodale) Wellenlänge und die spinodale Aufbruchzeit. Im Gegensatz zur Entnetzung von Flüssigkeit von einem festen Substrat kann sich auch die verborgene Grenzfläche verformen und die PS-Luft- als auch die PS-PMMA-Grenzfläche entwickeln sich gekoppelt. Die Amplitude der spinodalen Wellenlänge an den Grenzflächen ist mit der jeweiligen Grenzflächenenergie korreliert und die Amplitude der verborgenen PS-PMMA-Grenzfläche ist daher wesentlich größer als die der freien PS-Luft-Grenzfläche. Trotz der geringeren treibenden Kräfte im Vergleich zu PS-Filme auf SiO_2 ist die charakteristische Wellenlänge für PS-Filme auf PMMA-Substraten kleiner. Überraschenderweise wurde festgestellt, dass die anfängliche Rauheit beider Grenzflächen den Prozess der Modenauswahl beeinflussen kann, was die geringe Abweichung der experimentellen Ergebnisse von der theoretischen Modellierung auf Basis der linearen Stabilitätsanalyse erklärt.

Contents

1

Introduction

The stability of thin liquid films plays an important role in many technological applications that requires liquids to wet the substrate, for instance, paints to homogeneously coat a surface, lubricants to ease the movement of joints in mechanics of machines, adhesives to join two components or inks in printers. Wettability of liquids can be varied by manipulating the properties of liquids or substrates. Techniques such as plasma treatment and silanization manipulate the wettability of a substrate by modifying the chemical properties of its surface and so the surface tension [1]. The stability of thin films depends strongly on its thickness. If the thickness of a film is larger than the capillary length ($l = \sqrt{\frac{\sigma}{\rho g}}$), gravity is the dominating force and stabilizes the film on a horizontal substrate. However in extremely thin films where the interaction acts over length-scale of molecules, macroscopic forces such as gravity are negligible, short-ranged interactions are the dominating forces that determine the wetting behavior of liquids [2]. Thus, understanding and controlling of wetting and dewetting dynamics in nanoscale is necessary to design and fabricate surfaces for numerous applications in optoelectronics and biotechnology [3, 4, 5].

Much of the experimental and theoretical studies in dynamics of dewetting have involved polymer films, both because of their technological importance and due to high viscosity and low vapor pressure that allow for steady experiments with convenient time scales [6, 7, 8, 9, 10, 11]. The usual scenario for dewetting of polymers, whether on solid or liquid substrates, involves the formation of

holes. Dewetting in thicker films is typically initiated by nuclei in the form of dust particles or other surface heterogeneities and it is referred to as 'heterogeneous nucleation'. While another scenario for extremely thin films consist of the growth of capillary waves driven by Van der Waals forces across the film known as 'spinodal dewetting'. This was firstly studied by Vrij [12], Scheludko [13], Ruckenstein and Jain [14] and others in terms of the destabilizing effect of a disjoining pressure on the liquid interfaces that originate from Van der Waals forces, leading to many publications on the dewetting of thin polymer films [6, 7]. This type of dewetting is a powerful tool in determining the effective interfacial potential and Hamaker constant and it can be used in generating and controlling pattern formation in manufacturing functional layers in nano scale [15].

Dewetting of a polymer film from another polymer substrate where both polymers are in liquid state is more of a general case that involves a richer dynamics. Both the polymer-polymer interface and the polymer-air surface are deformable and are expected to evolve in a coupled way. In this system, parameters such as thickness and optical property of the two layers, viscosity ratio and interfacial tensions of the two liquids can play an important role for the dynamics and the evolving morphological structure of the interfaces [16, 15].

In this thesis the liquid-liquid spinodal dewetiing of a two layer polymer system is studied. The system consists of a thin layer of PS on top of a PMMA substrate that are supported by silicone wafer with a natural oxide layer. Dewetting is conducted by annealing the sample above the glass transition temperature of both of the polymers where the viscosity ratio of polymers are close to one and both of the polymers are in liquid state. We monitor the evolution of the morphology of the interfaces using Atomic Force Microscopy. In our sample the thickness of the PMMA layer is kept large enough to prevent the possible Van der Waals interaction of silicone or silicone dioxide with PS through PMMA layer in order to simplify the estimation of the effective interface potential.

The present work is structured as follows: in the chapter, *Background and*

State of the Art, we review the literature on the stability of polymers along with all the factors governing the wetting behavior. The experimental measurement techniques, the analyzing methods and the polymer properties are described in the *Material and Method* chapter. In the chapter, *Results and Discussions*, the experimental results on the evolution of the interfaces for different stage of dewetting is presented.

2

Background and State of the Art

2.1 Wetting and dewetting

Various industrial applications of liquids require them to spread evenly on a substrate. For instance, paints to homogeneously coat a surface, lubricants to ease the movement of joints in mechanics of machines, adhesives to join two components, inks in printers, etc. All of those applications require liquids to completely wet a substrate and remain stable, while one might be interested in manufacturing hydrophobic surfaces to avoid the substrate being wet by a liquid, for instance teflon coated pans or self cleaning surfaces. In either of theses applications, proper knowledge of the properties of liquids and substrates and the interaction of the involved phases in the system plays an important role in the final result. Wettability of liquids can be varied by manipulating the properties of liquid or substrate. Techniques such as plasma treatments and silanizing the substrate, can change the wettability of the substrate. By such treatments the chemical properties of the surface of the material can be modified and so the surface tension [1].

Even though the wettability is determined by the competition of surface tension forces with gravity on the macro scale [17], as the interaction acts over a scale of molecules where macroscopic forces such as gravity is negligible, short-ranged interactions that act in the range of tens of nanometers are the driving forces in
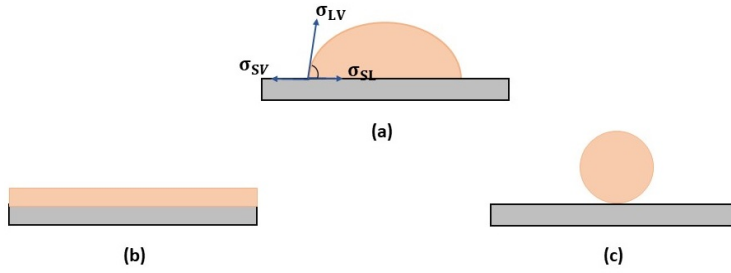
Figure 2.1: The three different wetting scenarios according to Young's equation.

wetting behavior of liquids. In such cases, in addition to the surface chemistry, surface forces such as Van der Waals or electrostatic forces are supreme for determining whether a fluid will wet a given substrate or not. The short range and long range microscopic forces are responsible for the equilibrium thickness of wetting films, and also are believed to be important for the way fluids spread over a solid surface.

The distinction between the different macroscopic wetting scenarios is usually made by considering the equilibrium spreading coefficient S_{eq}, defined as [2]:

$$S_{eq} \equiv \sigma_{SV} - (\sigma_{SL} + \sigma_{LV}). \tag{2.1}$$

The equation includes three surface tensions: solid-liquid σ_{SL}, liquid-gas σ_{LV} and solid-gas σ_{SV} that is associated with moist substrate. Here all the surface tensions are defined when the three phases: solid, liquid and gas, are in mechanical equilibrium (force balance) with each other. In addition, we consider chemical equilibrium and thermal equilibrium (temperature matching) between liquid and gas, so that the gas is the saturated vapor of the liquid and solid surface is placed on that atmosphere. Mechanical, chemical and thermal equilibrium together are referred to as thermodynamic equilibrium. If a liquid completely wets the substrate and system stays in thermodynamic equilibrium, the spreading coefficient is zero $S_{eq} \geq 0$.

We can categorize wetting regimes by Young's equation in equilibrium state, therefore For $\theta = 0°$,

$$\sigma_{SV} - \sigma_{SL} = \sigma_{LV},$$

the droplet will spread and will completely wet the substrate, see figure (2.1,

b). For $0°\langle\theta\langle180°$ one speaks of partial wetting (figure 2.1, a), and if $\theta = 180°$, then liquid does not wet the substrate and it is defined as non-wetting regime (figure 2.1, c). For the case where liquid partially wets the substrate, liquid will form a spherical cap and the macroscopic contact angle near the contact line is demonstrated as the in plane mechanical force balance defined with Young-Dupre equation in equilibrium state:

$$\cos\theta_{eq} = \frac{\sigma_{SV} - \sigma_{SL}}{\sigma_{LV}}. \tag{2.2}$$

However, this approach neglects possible interactions of the two interfaces of solid-liquid and liquid-vapor with each other, across the liquid film that come into play when the liquid thickness is in the range of intermolcular interactions of tens of nanometers. On that case, in the vicinity of the three phase contact line (the point where three phases meet), the interfaces can deviate considerably from a straight intersection at Young's contact angle and the equilibrium contact angle suggested by A. Frumkin [18] will be:

$$\Phi\left(h_{eq}\right) = \sigma_{lv}\left(\cos\theta_{eq} - 1\right). \tag{2.3}$$

The equation (2.3) links the effective interface potential ($\Phi(h_{eq})$) to macroscopic properties. Hence, if the surface tension σ_{LV} is known, the global minimum of the effective interfacial potential determines the contact angle [19].

2.2   Introduction to van der waals forces

Van der Waals forces are the weak electric forces that attracts or retards neutral molecules to one another and they exist between atoms or molecules in all the materials. Although they are the weakest chemical forces, they play important role in the molecular interactions in the range of $1 - 100$ nm distance between molecules and atoms. The van der Waals interaction fall into three sub groups regarding to the character of involved dipoles.

- Dipole-dipole force: molecules having permanent dipoles will interact by dipole-dipole interaction that is called also Keesom interaction.

- Dipole-induced dipole forces: the field of a permanent dipole induces a dipole in a non-polar atom or molecule.

- Dispersion forces: due to charge fluctuations of the atoms, there is an instantaneous displacement of the center of positive charge against the center of negative charge. Thus at a certain moment a dipole exists and induces a dipole in another atom. Therefore non-polar atoms or molecules attract each other.

The London interactions or dispersion interactions are initiated by temporary electromagnetic field produced by fluctuation of charges that arises spontaneously in material body or vacuum. The fluctuation of charges can be caused by thermal agitation and also quantum mechanical uncertainty in positions and momenta. Quantum mechanical presumptions emphasize that energy of electrons in an atom is never zero, therefore , it is constantly moving around its orbit and it is probable to find the electron anywhere in the orbital of an atom. Hence, the mobile electron can find themselves instantly on one end of atom or molecule, making that end negatively charged and then the other end with presence of nucleus, will be positively charged. The mobility of electron continuously can change the distribution of charge in atom and produces rapidly fluctuating dipoles even in the most symmetrical molecules such as noble gases. Therefore, If the distribution of charges in an atom is not symmetric, it will effect the neighbor atoms and will polarize them. The polarization depends on the time it takes for the electric field to travel from one atom to another one and back. If this time is comparable to the period of fluctuating dipole, the neighbor atoms will absorb the electromagnetic field imposed on them and they will be polarized accordingly. This induced dipole-dipole interaction where positively polarized side of an atom is attracted to negatively polarized side of the neighbor atom results in an attractive force for identical atoms. As long as atoms stay in proper distance from each other the polarities will continue to fluctuate in synchronization, so that the attraction is always maintained.
The Van der Waals forces have a long range characteristic, they fall off with distance according to a power law. The energy of attraction between two spheres with radius of R is proportional to R^{-6} that R is the distance between two bodies. If R is smaller or equal to the wave length corresponding to transition

between the ground and excited states of the atoms, the effect of retardation become important.

2.3   Instabilities

If the equilibrium contact angle of a liquid on a substrate is θ_{eq}, it partially wets the surface. Therefore, if we prepare a thin film of liquid by spin coating on the substrate or transfer it on the substrate, the film is not stable and if the requiered energy is provided, it will dewet from the substrate, decaying into droplets with a finite contact angle of θ_{eq}. Dewetting can be caused by several reasons that the different dewetting pathways on thin polymer films is discussed at next section.

As explained in the former section, if a liquid droplet is deposited on a substrate that energetically is in favor of wetting, the droplet spreads and forms a thin layer of liquid on the substrate with a finite thickness, determined by interfacial forces and it eventually will be in minimum steady state of energy. Assume, that a liquid such as polymer in its liquid state, does not initially wet the substrate and a thin layer of polymer film is prepared by a non-equilibrium technique such as spin coating. On that case with annealing the polymer above the glass transition temperature where it is in liquid state, the polymer film will dewet from substrate forming dry spots. Note that dewetting of thin polymer films depends strongly on the thickness of polymer layer. If the thickness of film is larger than the capillary length defined as:

$$l = \sqrt{\frac{\sigma}{\rho g}},$$

where ρ is the density of polymer and σ is the surface tension, then gravity force dominates and stabilizes the film. For the thicknesses below l, however, the gravity effect is negligible [20] and the stability of a thin film in the range of tens of nanometer is governed by the effective inter-facial potential (Φ) as a function of film thickness. It comprises both repulsive short-range and attractive long-range interactions (attractive Van der Waals part and repulsive part) and it is defined as the excess free energy per unit area, necessary to bring

two interfaces from infinity to a certain distance of h [21]. For the description of Van der Waals forces of a composite substrate, the layer thickness and their respective polarization properties have to be taken into account [22]. The stability of thin film is distinguished in three major states of stable, meta stable and unstable sate of energy, see figure (2.2).
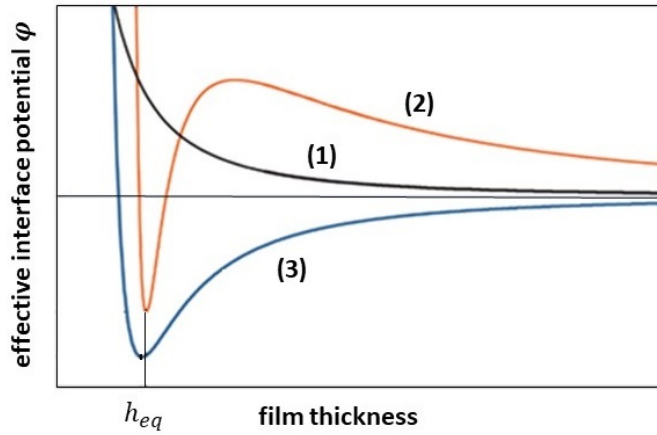

Figure 2.2: Schematic presentation of effective interfacial potential as function of film thickness [23].

The curve (1) characterizes a stable film that perfectly wets the substrate. Since energy would be necessary to thin the film, the equilibrium film thickness is infinite. The two other curves exhibit a global minimum of $\Phi(h)$ at $h = h_{eq}$ indicating that system is in unstable state of energy and it can minimize its energy, reaching the equilibrium thickness. The wettability of the substrate by the liquid is correlated to the depth of the minimum at $h = h_{eq}$. The deeper the global minimum of Φ, the larger is the equilibrium contact angle of the liquid on the surface. The curve (2) characterizes a film that is metastable containing a potential barrier that the system had to over come to reduce its energy and reach equilibrium film thickness h_{eq}. Within the stable region of curve, any defects or dust particle or impurities in the film or homogeneity of the substrate, can cause instabilities and initiating dry spots (holes), called heterogenous nucleation, see figure (2.3, c). If the nucleation is caused by dirts or dust particles, an object could be observed right in the center of a hole by light microscopy or atomic force microscopy in rare cases and the number of

nuclei can be reduced by improving the preparation conditions.

In addition, at the edge of the linearly unstable region (curve 2), where the curve changes sign on the deflection point, thermal fluctuations can over come the energy barrier, leading to the minimum energy [24]. On that case, improving the preparation conditions is not effective in reducing the number of nuclei, implying that the cause of nucleation can be more than just defects or contamination (figure 2.3, b). Seemann [19] proposed that the possible cause of nucleation could be the strain in the films induced by the preparation procedure. A typical way for the preparation of a thin polymer film is to spin coat it on a smooth substrate. During spinning, the solvent evaporates and leaves a thin layer of polymer behind. The radius of gyration r_g of the polymer immediately after spin coating is larger than r_g for the polymer melt. So probably rearrangement of the chain to achieve the r_g of the melt polymer is the reason for nucleation. So, annealing the polymer above the glass transition temperature on a substrate that polymer is stable and does not dewet, would be helpful to relax the polymer chains and decrease the density of holes.

The last scenario of dewetting is possible for extremely thin liquid films, and it is caused by unstable growth of capillary waves that are amplified by molecular forces across the film leading to the rupture of the film. The considered mechanism leading to the symmetry breaking of the initially flat film is called spinodal dewetting [25]. The spinodal rupture of a free liquid film results in the dewetting pattern of hills and gullies with a preferred distance λ, so called spinodal wavelength. The spinodal wavelength λ and rupture time τ are the two factors to identify a spinodal dewetting process in experimental systems [26].

The spinodal wavelength is linked to the effective interface potential with

$$\lambda\left(h\right) = \sqrt{\frac{-8\pi\sigma}{\Phi"\left(h\right)}}. \tag{2.4}$$

As you see from equation (2.4), the spinodal dewetting has a rational solution if the second derivative of the effective interfacial potential with respect to film thickness is negative, $(\Phi"(h)\langle 0)$.
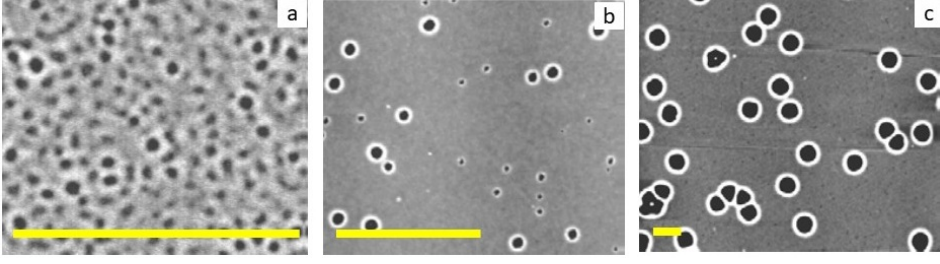
Figure 2.3: AFM images of dewetting PS ($2\frac{kg}{mol}$) films. Scale bars indicate $5\mu m$; the z-scale ranges from 0 (black) to 20 nm (white). Panel a, 3.9 nm PS on a Si wafer with an oxide thickness of 191 nm. Panel b, 4.1 nm PS on a wafer with an oxide thickness of 2.4 nm. Panel c, 6.6 nm PS on a wafer with a 1.7 nm thick oxide layer. Images are taken from [23].

While Young's contact angle is only defined for the equilibrium state, it is related to the depth of effective interfacial potential by equation (2.5). A. Frumkin [18], published the relation between effective potential and the contact angle as:

$$\Phi\left(h_{eq}\right) = \sigma_{lv}\left(\cos\theta_{eq} - 1\right).$$ (2.5)

The consequence of the two equations (2.4) and (2.5), is to determine the wavelength λ as a function of film thickness h, enabling us to gain the course of $\Phi''(h)$. By additionally measuring the equilibrium film thickness h_{eq} and the contact angle θ, it is possible to reconstruct the complete effective interfacial potential defined as:

$$\phi_{Total}\left(h\right) = \frac{c}{h^8} - \frac{A}{12\pi h^2}$$ (2.6)

Equation (2.6) contains two terms [21], the short range and the Van der Waals terms that are characterized by different exponents and different interaction constants. The short range repulsive forces are effective in the range of a few angstroms where the repulsion is due to the overlapping of electron shield of two bodies with distance of h and is described by a higher-order polynomial function and varies as h^{-12}. Considering two planar surfaces, this repulsion yields an interaction energy varying as

$$\Phi_{steric}\left(h_{eq}\right) = \frac{c}{h^8}$$ (2.7)

where c is a constant characterizing the interaction strength [27]. For an extended derivation of the equations we like to refer to J. Israelachvili's approach [28]. The second term in the effective interfacial potential is the Van der Waals interactions between two atoms that varies as h^{-6} in the non-retarded approximation. The non-retarded interaction yields

$$\Phi_{vdw}\left(h\right) = -\frac{A}{12\pi h^2} \tag{2.8}$$

for two planar surfaces where A is the Hamaker constant. If A is positive the Van der Waals interaction between two bodies is attractive and in case of negative A, the interaction will be repulsive. The Van der Waals interaction of two media through a third medium can be determine by the sign of magnitude and sign of Hamaker constant using the equation (2.9) [28].

2.3.1   Hamaker constant

The Hamaker constant caculated on the basis of Lifshitz theory is given by equation (2.9). The Lifshitz theory of van der Waals is based on considering the macroscopic properties of the media. The attraction was assumed to be due to a fluctuating electromagnetic field in the gap which arises due to the spontaneous electric and magnetic polarization within the media. It is important for the gap to be larger than molecular dimensions. The media were treated as continuous and the force between the macroscopic bodies was derived in terms of the dielectric constants and refractive indices. This theory is particularly suitable when we want to calculate the Hamaker constant for the interaction of the media 1 and media 2 across medium 3. Assuming the absorption frequency of all three media are the same, the approximated estimation for the non-retarded Hamaker constant is according to equation (2.9).

$$
\begin{aligned}
A_{Total} &= A_{\nu=0} + A_{\nu>0} \\
&\approx \frac{3}{4}kT\left(\frac{\varepsilon_1-\varepsilon_3}{\varepsilon_1+\varepsilon_3}\right)\left(\frac{\varepsilon_2-\varepsilon_3}{\varepsilon_2+\varepsilon_3}\right) \\
&+ \frac{3h\nu_e}{8\sqrt{2}}\frac{\left(n_1^2-n_3^2\right)\left(n_2^2-n_3^2\right)}{\left(n_1^2+n_3^2\right)^{\frac{1}{2}}\left(n_2^2+n_3^2\right)^{\frac{1}{2}}\left\{\left(n_1^2+n_3^2\right)^{\frac{1}{2}}+\left(n_2^2+n_3^2\right)^{\frac{1}{2}}\right\}}
\end{aligned}
\tag{2.9}
$$

The first term, $A_{\nu=0}$ characterizes the purely entropic contribution to the total Van der Waals pressure. The zero frequency force is raised due to the thermal agitation of permanent electric dipoles present in the three media and includes Debye and Keesom contributions. For reasons of consistency with the following treatment of the quantum mechanical dispersion contribution, the material properties are all incorporated into the so called "entropic Hamaker constant". It should be noted that the latter quantity can not exceed a value of $\frac{3}{4}\zeta KT$, (ζ, denotes Riemann's ζ function) which is about 3.6×10^{-21} or 22.5 meV at $T = 300K$ and K is the Boltzmann constant ($1.3 \times 10^{-23}\frac{m^2 kg}{s^{-2}K^{-1}}$). For the interaction through vacuum where the dispersion energy contribution is typically $\approx 10^{-19}J$, this is always negligible, but for interactions across the medium, zero frequency contribution sometimes dominates over the dispersion energy contribution. The second term is a function of the London dispersion forces that depends on the orbiting electron frequency (ν_e), the refractive index n and dielectric constant ε of the material. ν_e is the main electronic absorption frequency in the ultra violet region. Its value usually lies between $3 \times 10^{15} s^{-1}$ and $5 \times 10^{15} s^{-1}$. Accordingly the Van der Waals forces between two identical bodies in a medium is always attractive (A positive), while that between different bodies in a medium, it can be attractive or repulsive.

The Hamaker constant for two similar media interacting across another medium remains unchanged if the media are interchanged. Thus if no other forces are operating, a liquid film in air will always tend to thin under the influence of the attractive Van der Waals forces between the two surfaces, or in other words, two air phases, such as bubbles, attract each other in a liquid.

In a two layer polymer system of our interest that includes a thin layer of PS on top of PMMA, based on the dielectric properties of PS and PMMA [29, 30], the Hamaker constant for the two interfaces system consisting of air-PS-PMMA can be calculated to $(-1.49 \pm 0.002) \times 10^{-20}\frac{J}{m^2}$. To calculate the Hamaker constant all media are taken as being dielectric with a single electronic absorption frequency being in the range of $3 \times 10^{15} Hz$ [28]. The dielectric constants of air, PS, and PMMA respectively are considered as

1.00059, 2.6, and 2.6 [30]. The refractive indices of air, PS, PMMA are 1.00029, 1.5894, and 1.4893, respectively [30]. This negative Hamaker constant means that a PS film on top of a PMMA substrate is spinodally unstable, leading to amplification of the amplitude of the preferred wavelength and potentially spinodal film break up and hole formation. If the order of polymers change in our samples, i.e. PMMA on top of the PS will be stable. In addition to simplify the calculation of Hamaker constant we prepare PMMA above 100 nm, that is thick enough to shield the possible interaction of silicone wafer or silicone dioxide with PS through PMMA film.

2.4 Theory of thin film stability

The dynamic properties of capillary waves and the stability of thin films was investigated by Cahn [31] and Vrij [12] and Vrij was the first to include Van der Waals forces in the stability analysis of soap films. Assume a typical thin film as a liquid layer on a substrate with a free surface where the liquid is exposed to air (or a gas) or another fluid that has a thickness of h_0, much smaller than the lateral dimension of the film, as a result, the flow of liquid takes place mainly in the lateral direction that is parallel to the substrate.
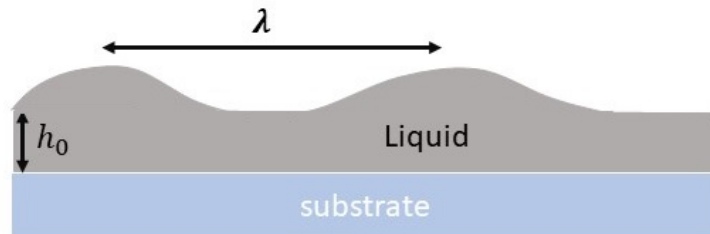

Figure 2.4: schematic of capillary waves formation on a liquid-air interface.

In analyzing the development of instabilities, initially presence of certain wavelengths are taken into account that some would grow while others decay. In the linear stability analysis, the thermal perturbations (capillary waves) that initiates the instabilities are assumed to be sinusoidal in shape that can be give by equation (2.10):

$$h(x,t) = h_0 + \zeta e^{iqx + \frac{t}{\tau}} \tag{2.10}$$

where h_0 is the thickness of liquid film, ζ is the amplitude of capillary waves, q the wave vector and τ is the rupture time.

The liquid flow is governed by Navier Stokes equation and since the thickness of the film h_0 is much smaller than the planar dimensions, the problem is approximated by lubrication theory[32].

$$\rho(\frac{\partial v}{\partial t} + (v.\nabla)v) = -\nabla p + \eta\nabla^2 v + \rho g \tag{2.11}$$

where ρ is the density, v the velocity, p the pressure and η the viscosity of the flow. In case of non-volatile fluid, the fluid density ρ is constant with time ($\frac{\partial \rho}{\partial t} = 0$) and the fluid is incompressible. In addition the continuity equation requires the material flux in all direction to be constant,

$$\frac{\partial \rho}{\partial t} + \rho\nabla.v = 0$$

Flow of polymers with high viscosity takes place in low Reynolds Number regime,

$$(\frac{\rho(v.\nabla)v}{\eta\nabla^2 v}) \ll 1$$

where the inertia term in the Navier Stokes equation is smaller than the viscous term and can be ignored. For the thin films with thickness below the capillary length (l) the velocity variation in the lateral direction is smaller than vertical direction,

$$\frac{\partial v}{\partial x}, \frac{\partial v}{\partial y} \ll \frac{\partial v}{\partial z}$$

as a result the second derivatives of the velocities in x and y direction can be neglected and in the end the Navier Stokes equation can be approximated by

$$-\nabla p + \eta\nabla^2 v = 0. \tag{2.12}$$

To simplify equation (2.12) further, we can ignore the pressure gradient ($\frac{\partial p}{\partial z} = 0$) in vertical direction for the low thickness and pressure gradient is assumed to depend on the lateral coordinates, leading to

$$-\frac{\partial p}{\partial x} + \eta\frac{\partial^2 v}{\partial z^2} = 0. \tag{2.13}$$

One can continue with the equation by integrating along the z-axis and the velocity is obtained as:

$$v = \frac{1}{2\eta}\frac{\partial p}{\partial x}z^2 + az + b \tag{2.14}$$

By inserting the boundary conditions the variables (a and b) can be obtained. For example assuming the no slip boundary condition on the substrate ($z = 0$), the velocity of fluid at the liquid-solid interface is zero, then ($b = 0$). On the liquid surface ($z = h$), The flow is stress free and the velocity of liquid components is zero ($v = 0$), then ($a = -\frac{1}{2\eta}\frac{\partial p}{\partial x}h$), that leads to

$$v = \frac{1}{2\eta}\frac{\partial p}{\partial x}(z - 2h)h. \tag{2.15}$$

The average velocity is obtained by integrating along the z-axis from 0 to h,

$$U = \frac{1}{h}\int_0^h vdz = \frac{h^2}{3\eta}(-\frac{\partial p}{\partial x}) \tag{2.16}$$

The resulting one-dimensional flux (ξ) through a surface $A = h$ is given by,

$$\phi = A \times U$$

$$\xi = \frac{h^3}{3\eta}(-\frac{\partial p}{\partial x}). \tag{2.17}$$

Equation (2.17) describes the velocity profile in the liquid film. The velocity profile also introduces the volume conservation that In case of one dimension flow, this means that any change in volume is accompanied by a change in the film thickness.

$$\frac{\partial h}{\partial t} + \frac{\partial \xi}{\partial x} = 0 \tag{2.18}$$

Combining equation (2.17) with equation (2.18), the equation of motion for the thin film of a liquid on solid substrate with no slip on the substrate is obtained as:

$$\frac{\partial h}{\partial t} = \frac{\partial}{\partial x}(\frac{h^3}{3\eta}\frac{\partial p}{\partial x}). \tag{2.19}$$

Considering the first assumption that the capillary waves forms on the free surface of a liquid film, the surface forms a wave structure that the curvy structure of the surface generates Laplace pressure (P_L). The Laplace pressure tends to stabilize the film by damping the perturbations. The Laplace pressure is related to the surface tension and the curvature of the surface by:

$$P_L = -\gamma \frac{\partial^2 h}{\partial x^2}. \tag{2.20}$$

In addition to the stabilizing contribution of Laplace pressure to the equation of motion (2.19), we add the contribution of destabilizing forces that can be Van der Waals forces, electrostatic forces, etc,. We add this term as disjoining pressure Π and the equation of motion of liquid-air interface is given by equation (2.21),

$$\frac{\partial h}{\partial t} = \frac{\partial}{\partial x} \left(\frac{h^3}{3\eta} \frac{\partial(P_L + \Pi)}{\partial x} \right). \tag{2.21}$$

We continue with taking the derivatives and substitution of the Laplace pressure that leads to

$$\frac{\partial h}{\partial t} = \frac{\partial}{\partial x} \left[\frac{h^3}{3\eta} \frac{\partial}{\partial x} \left(-\gamma \frac{\partial^2 h}{\partial x^2} + \Pi \right) \right] \tag{2.22}$$

Considering equation (2.10), if the amplitude of capillary waves are much smaller than the film thickness ($\zeta \ll h_0$), higher orders of the gradient of h ($\frac{\partial h}{\partial x} \propto \zeta$) can be neglected and the equation simplifies to

$$\frac{1}{\tau} = -\frac{h^3}{3\eta} \left[\gamma q^4 + q^2 \frac{\partial \Pi}{\partial h} \right] \tag{2.23}$$

where $q = \frac{\partial h}{\partial x}$ [33].

In case of a thin polymeric liquid film on a solid substrate, the equation suggests the exponential growth of all the stabilizing and destabilizing modes and the one that grows the fastes will dominate the other modes.

For more complex systems, such as the two layer polymer system that the substrate is also liquid, one need to study the growing mode on liquid-liquid interface in addition to liquid-air interface, and to the procedure for both of the interfaces that we would like to refer to [16, 34] for further studies.

3

Material and Method

3.1 AFM

Atomic Force Microscopy (AFM) is the most widely used form of Scanning Probe Microscopy (SPM), since it requires neither an electrically conductive sample, as in Scanning Tunneling Microscopy (STM), nor an optically transparent sample or substrate, as in most Near field Scanning Optical Microscopes (NSOM). Basic AFM modes measure the topography of a sample with the only requirement being that the sample is deposited on a flat surface and rigid enough to withstand imaging. Since AFM can measure a variety of forces, including Van der Waals forces, electrostatic forces, magnetic forces, adhesion forces and friction forces, specialized modes of AFM can characterize the electrical, mechanical, and chemical properties of a sample in addition to its topography.

The simplest imaging mode is the so called contact mode that the tip is attached to a small cantilever (figure 3.1). A laser spot is reflected off the backside of the cantilever onto a photo diode. As the tip goes over features, the cantilever will be deflected, altering the vertical location of the reflected spot on the detector. To achieve more controlled imaging conditions, a feedback loop monitors the tip-sample force. The system's feedback loop operates in the usual manner using changes in the cantilever's deflection and adjust the cantilever Z-position to hold the force constant and Topography is taken by

converting the vertical location of the laser spot on photo diod to a height. Heights can be measured down to sub-nanometer and up to 8μ (AFM used for our measurements). The contact mode is generally only used for flat samples that can withstand lateral forces during scanning.

In the intermediate contact mode (tapping mode), during scanning over the surface, the cantilever oscillates sinusoidal in air at its resonant frequency. As the cantilever moves vertically, the reflected laser beam, or return signal, deflects in a regular pattern over a photo diode array, generating a sinusoidal electronic signal, whereas the amplitude depends on the (average) distance between tip and sample, see figure (3.1). Although the piezo stack continues to excite the cantilever with the same energy, the tip deflects in its encounter with the surface and the oscillating tip slightly taps the surface at the resonant frequency of the cantilever with a constant oscillating amplitude. The oscillating amplitude is kept large enough so that the tip does not get stuck in the sample because of adhesive attractions. The tapping mode is used in topography measurement to minimize effect of friction and other lateral forces to measure the topography of soft surfaces. The cantilever motion can be characterized by its phase relative to a driving oscillator. When the tip hits the surface, the energy stored in cantilever converts partially to heat and potential energy of materials. The phase shift can be thought of as a delay between the oscillation of the driver and the oscillator.

The Phase shifts are registered for each scan point as bright and dark regions in phase image. Phase imaging can provide information about variations in composition, adhesion, friction, visco- elasticity, and other properties, including electric and magnetic properties. The phase signal is sensitive to both short and long-range tip-sample interactions. Short-range interactions include adhesive forces and frictional forces; long-range interactions include electric fields and magnetic fields. The applications of phase imaging include locating contaminants, mapping different components in composite materials, and differentiating regions of high and low surface adhesion or hardness as well as regions of different electrical or magnetic properties. It allows chemical mapping of surfaces based on these material differences. It is particularly useful in analyzing polymers, composites, and surface coatings. NanoScope brand
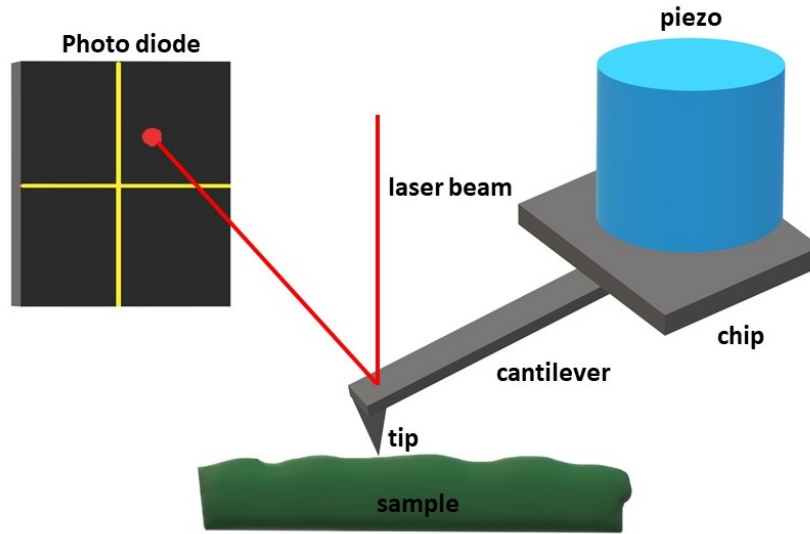
Figure 3.1: Schematic of an AFM

AFMs allow capturing both height (topography) and phase data simultane-
ously allowing surface structure and material domains to be directly compared.
Quantitative analysis for phase imaging is very difficult, because it is related
to the amplitude setpoint, tapping frequency, etc., so it is usually used only
for qualitative analysis of surface mechanical properties. Image (3.2) reveals
phase imaging e that demonstrates the material contrast of a polymer with
dewetted holes on top of another polymer. Inside the holes, has higher phase
shift comparing to the rest of the image, meaning that the driving frequency is
higher than the resonant frequency on those spots and in fact the underlying
polymer is stiffer than the upper layer polymer. We benefit from phase images
qualitatively to determine the moment, when the polymer layer breaks up
and dewets from the substrate. Note that we can not quantify the mechanical
properties using phase shifts and one is better to use Peak Force Microscopy
for that purpose.

3.1.1   Peak Force Microscopy

Peak Force Microscopy, Quantitative Nano Mechanics (QNM) mode is an
extension of Peak Force Tapping Mode that enables quantitative measurement
of Nano-scale material properties such as modulus, adhesion, deformation and
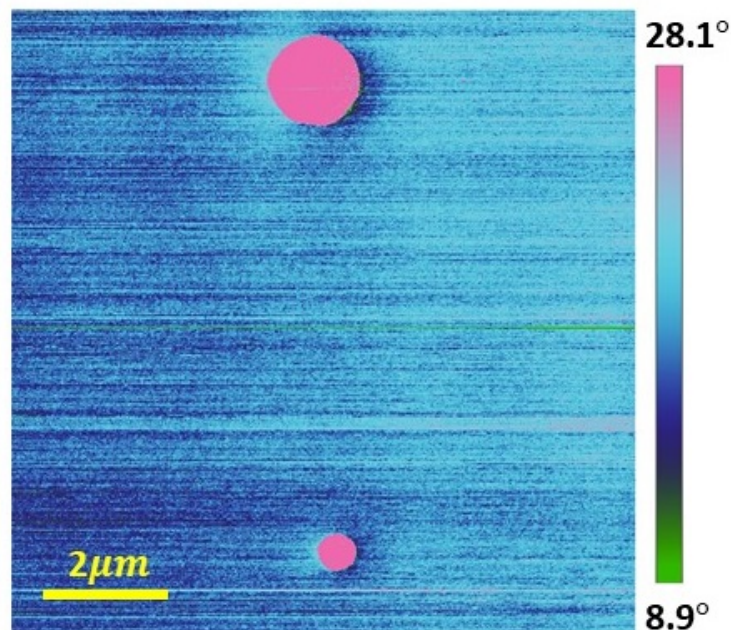
Figure 3.2: The phase image of polymer surface, captured in situ at $131°C$, soft tapping mode by AFM. Circular geometry demonstrate dewetted holes on the polymer surface.

dissipation. Peak Force Tapping mode imaging increases the resolution by controlling the force that the tip applies to the sample. Every time the tip touches the surface, a force distance curve is obtained and therefore parameters like elasticity, adhesion, and deformation can be recorded at every scan point. The cantilever at Peak Force Tapping mode oscillates, but far below its resonant frequency, thereby it decreases the deformation depths and consequently the contact area between the tip and sample decreases. Since the deformation depths and lateral forces are small, there is minimal damage to the tip or sample. Image (3.3) shows an example that demonstrates the adhesivity of two different polymer films in comparison to the topography signal (3.3, a), that one of the polymers is partially lying on top of the other. As you see on figure (3.3, b) the different adhesion property of polymers is being reflected in the scale of Newton and it is the applied adhesion force between th tip and the substrate. Panel a, is the topography image of scanned area where the left side with darker color belongs to lower layer and the right side with brighter color belong to the top layer.
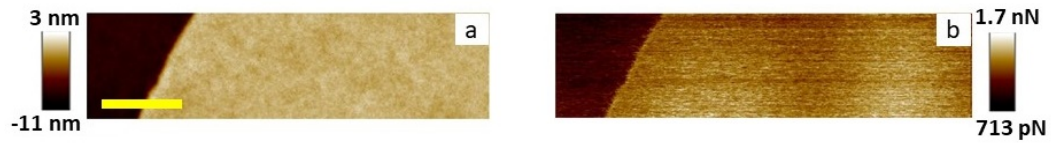
Figure 3.3: The topography (panel a) and adhesion (panel b) image of Polystyrene layer on top of a Polymethylmethacrylat layer, captured ex situ at room temperature, by Peak Force Microscopy mode. The thickness of PS is 14 nm. Scale bar presents $1\mu m$ on the sample.

In this mode, force-distance curve are obtained that explains the whole circle of each tap and you can find the sketch on figure (3.4). The blue color sketch the approaching path and the red line sketch the retraction path. The horizontal axis gives the distance that the piezo travels in Z distance in order to approach or to retract from the surface, and the vertical axis gives the tip deflection. At the beginning the piezo extends and the tip approach the surface, which is in this point in free air and hence shows no deflection. This is indicated by the flat portion of the curve. As the tip approaches within a few nanometer of the sample (point.1), an attractive force exists between the atom of the tip surface and the atom of the sample surface. The tip is pulled toward the sample and contact occurs at point (2), from this point on, the tip is in contact with the sample surface, and as the piezo extends farther and the maximum force is applied, the tip gets deflected farther to point (3). This is represented by the slop portion of the curve. As the piezo retracts, the tip goes beyond the zero deflection to point (4) and due to attractive Van der Waals forces and long range meniscus forces, it goes into the adhesive regime at point (5) on the retract plot, where the minimum deflection point is the maximum adhesion force. Later on, the tip snaps free of the adhesive forces and is again back in free air at point (6). The horizontal distance indicated by green arrow, along the retrace line gives the distance the tip moves in the adhesive regime. This distance multiplied by the stiffness of the cantilever gives the adhesive force. Incidentally, the shift or the difference between the loading and unloading curves (yellow region) results from the hysteresis in the piezo. Similar performance as described, done in a high speed and force curve, is achieved for every pixel and the peak interaction force of each of these force curves is then used as the imaging feedback signal that one example discussed

at firgure(3.3) .
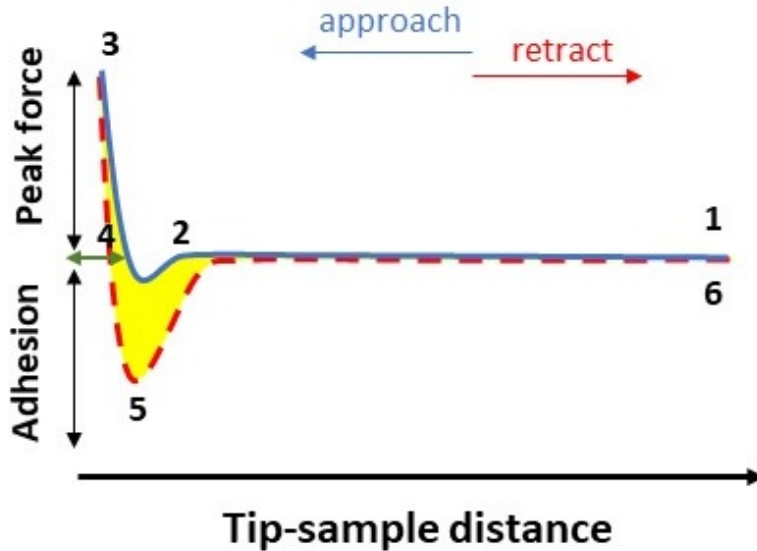
Figure 3.4: schematic of the tip motion during single approach in QNM mode.

The source of the adhesion force can be any attractive force between the tip and the sample, for instance, Van der Waals, electrostatics, and forces due to the formation of a capillary meniscus can all contribute and their contribution depends on the strength of each of them that it depends on parameters such as Hamaker constants, surface charges, and hydrophilicity. For example, if either sample or the probe surface is hydrophilic, a capillary meniscus will typically form, leading to higher adhesion that extends nanometers beyond the surface. For liquid polymers in which the long molecules serve as a meniscus, the adhesion can extend tens of nanometers beyond the surface. By increasing the tip radius, the contacting surface area is increased and consequently the adhesion increases [35].

3.1.2 Nano-manipulation

In study of the interfaces, we often need to monitor the evolution of one spot in different time scales or after removal or adding the top layer on the substrate. Such experimental approaches require finding the initial spots and giving the nanometric scale of the patterns on the interfaces, any error would interfere

with correlating the interfaces and the result of the analysis. For that purpose,
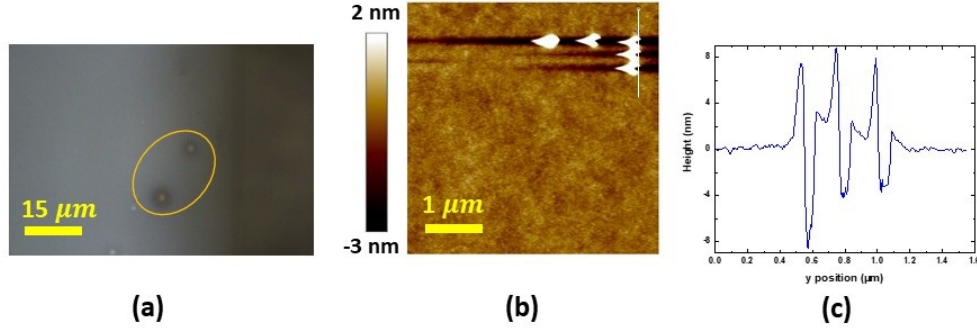
Figure 3.5: Reference points on a polymer surface in finding a certain spot. Panel a, microscopic image of the polymer surface that the optically visible signs are shown inside the yellow ellipse. Panel b, marks made by AFM tip. Panel c, the height profile of the white line on the image in panel b.

we first use signs that are optically visible as a reference points to find the vicinity of the targeted spot. Those signs can be made by scratching on the sample with sharp tools or it could be any dirt particles or cracks on the sample (see figure 3.5, a). Then we need smaller marks that are visible on the image captured by AFM but in a very small size that do not disturb the rest of the image, see figure (3.5, b).

We benefit from nano-manipulation mode of the AFM that is designed for nanolithography. By this program, one can technically write on a surface by proper setting according the softness of the surface and structure of the AFM tip. In our experimental system that sample is consist of polymer layers, there will be large amount of raised particles giving the softness of the polymer material that contaminates the rest of the scanning area. To avoid such problem, we mark the desired spots with only one time engaging the AFM tip creating dots with a certain bepth (see figure 3.5, c). The depth of the marks is controlled by setting a parameter, called z-distance. The higher the value of the z-distance, the deeper the marks are. In addition, the deeper marks have larger size since the AFM tips are usually sharper in the ending and the diameter of the tip increases with distance from the ending (figure 3.1).

3.1.3 Cantilever and the tip

The AFM tips are usually fabricated out of a silicon. Besides silicon or silicon nitride, it can be built from diamond, carbon nanotubes or plastics, with various geometries. Longer cantilevers have lower spring constants and therefore offer greater sensitivity for most samples. Shorter cantilevers afford better control when applying strong attractive forces and are less prone to over engage in materials by surface tension forces. Sharper tips are more likely to plastically deform the sample, and are less sensitive to adhesive force, than the tips that are more blunt. The cantilevers used for all the AFM data presented in this thesis have resonant frequency of $300kHz$ and spring constant of $26.1\frac{N}{m}$. The tip has a shape of Tetrahedral with an asymmetric side profile with a tip angle of 35°. Then the cantilever chip is attached to a chip holder with an angle about 10°.

3.2 Ellipsometry

Ellipsometry is a very sensitive optical method, used for about a hundred years to derive information about surfaces. The measurement principle is based on the fact that polarized light changes its polarization state (orientation and ellipticity), when being reflected from the surface of a sample. Change in the polarization presented as (Ψ) and (Δ) values, is used to calculate the optical constants of a material or to determine thickness and optical property of a surface. If the surface is covered by a thin film or a stack of films, the entire optical system including film and substrate, affects the polarization. On that case, multiple reflection at the interfaces of the layers superimpose to finally form the reflected light with an altered state of polarization.

The main optical components used for ellipsometers are laser, polarizers and compensators. A polarizer is a component that produces the linearly polarized light coming from laser to a light with special state of polarization at the output according to the rotational angle of its axis. Beside the polarizer there is an optical retarder called compensator which is quarter-wave plate that has a fast and low axis leading to a phase shift. If the angle of compensator is set to 45°
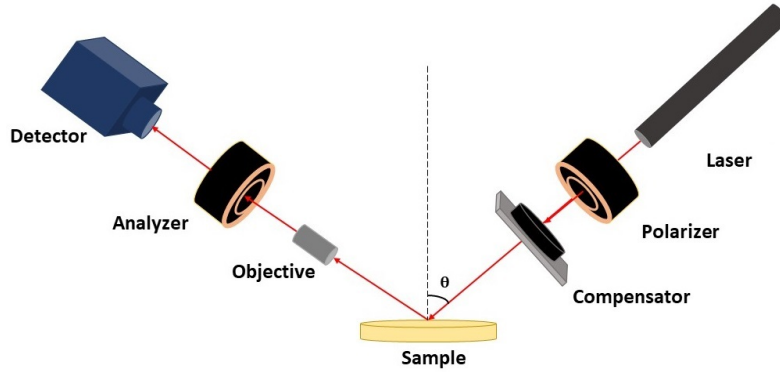
Figure 3.6: Schematic of a Nulling-Ellipsometer

in respect to the angle of polarizer axis, it transforms the ellipse of polarization into circularly polarized light. Upon reflection from the sample surface, the size and shape of the ellipse of polarization is changed and the transmitted intensity to the detector will depend on the polarization angle of the incident light. In fact analyzer only allows the light that is polarized along its axis to reach the detector [36].

The differences between the various instruments are mostly due to the choice of polarizer and analyzer and the light source but in principle they all are doing the same job. We used $EP3$ model of Occurion and the multiscope designed by Optrel GBR to measure the polymer film thicknesses in this thesis.

3.3 Analysis

Characterizing the pattern formation on both of the interfaces in two layered polymer system is the key in quantifying the deformations of interfaces during dewetting process. The precise analysis requires proper technique, suitable for different stage of dewetting. In This thesis, we benefit from Power spectral density (PSD) and pair correlation function (PCF), based on the suitability of the one for the existing pattern. In this section the details of each technique is briefly discussed and their efficiency is studied with examples.

3.3.1 Pair Correlation Function (g(r))

Pair correlation function is the probability of finding the center of a particle with a given distance from the center of another particle in a system. The probability is related to how the particles are packed together and in a more dense system it is more likely to find two or more of them with a given distance.

$$g(r) = \frac{V}{4\pi r^2 N^2} \left(\sum_i \sum_{j \neq i} \delta\left(r - r_{ij}\right) \right) \tag{3.1}$$

The equation (3.1) is the way to calculate pair correlation function g(r) as a function of distance in a volume. If r is the position of center of a particles, then r_{ij} is the position of center of surrounding particles . N is the total number of reference particles. V is the volume of the spherical shell that counts as all the particles surrounding the reference particle. Result of computation will be distribution of particles as a function of distance.

(a)   (b)
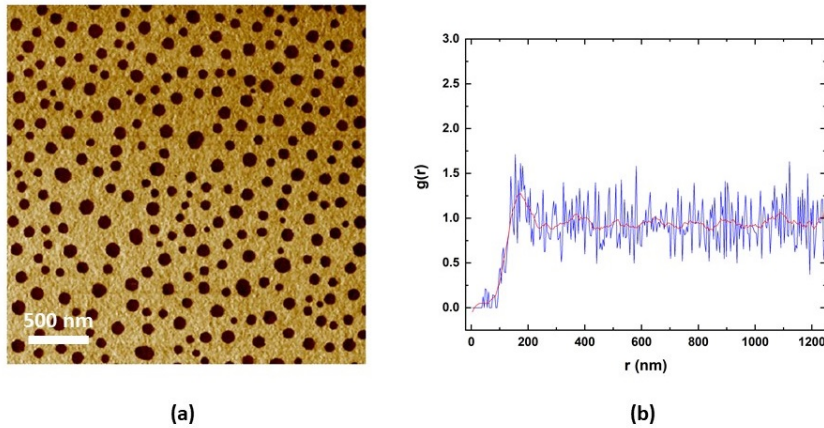
Figure 3.7: Example of pair correlation function analysis. Panel a is the phase signal of dewetted droplets on a polymer surface captured by AFM and panel b demonstrate corresponding pair correlation function analysis (blue line). Red line is a smoothing function fitted on original data.

Figure (3.7) is an example, containing dewetted droplets on a polymer surface captured by AFM. At first, we provide the position of center of droplets on the image using desired software as the input, then the preferred distance between droplets is calculated by pair correlation function (equation 3.1). The

first peak, presenting the most repeated distance between holes on figure (3.7, b) is roughly 200 nm, which is the estimated distance between holes, reading the scale bar on figure (3.7, a).

3.3.2   Power Spectral Density

The Power Spectral Density (PSD) function is useful in analyzing the repeated patterns on the surface. It provides a representation of the amplitude of a surface roughness as a function of the spatial frequency of the roughness. Spatial frequency is the inverse of the wavelength of the roughness features. The PSD function reveals periodic surface features that might otherwise appear random and provides a graphic representation of how such features are distributed. Power spectrum is a plot of power as a function of spatial wavelength or frequency. We use the PSD analysis that is implanted in software of the Nanoscope analysis to study the pattern signals on the polymer interfaces. As an example on how PSD analysis operates, we would like to refer the example that Brucker company has published, using Nanoscope analysis software, see figure (3.8).

Figure 3.8: Panel a is the topography image of Epitaxial Gallium Arsenide, captured by AFM. Panel b is the corresponding PSD analysis. The Arrow shows the location of peak, presenting wave length of repeated pattern [37]

3.4   Roughness

A detailed information such as smoothness and wettability of substrate in combination with right choice of the polymer solvent and proper spin coater and etc, has key role preparing smoother polymer interfaces. Hereby, we discuss

Interface	Si-air	Mica-air	PMMA-air	PS-air
R_q (nm)	0.20	0.27	0.28	0.17
R_{max} (nm)	3.72	2.97	2.5	1.69

Table 3.1: Roughness values of all the interfaces involved in our two layer polymer system. Extracted from AFM image with similar size and similar resolution, captured at room temperature.

the roughness of all the interfaces involved in the preparation of polymer interfaces. To quantify the roughness of all the surfaces that play a role in the roughness of interfaces in our two layer polymer system, we scanned each of the surfaces using AFM, soft tapping mode in room temperature. The size and resolution is kept constant for all the images, see figure (3.9). The roughness value will be discussed as the root mean square average of height deviations taken from the mean image data plane, expressed as:

$$R_q = \sqrt{\frac{1}{MN} \sum_{m=1}^{M} \sum_{n=1}^{N} (z(x_m, y_n) - \langle z \rangle)^2} \tag{3.2}$$

Figure (3.9) demonstrates the topography of interfaces, where panel a) is the topography of silicone-air interface with natural oxide layer of 2 nm, panel b) shows the topography of Mica-air interface, panel c), is the topography of PMMA-air interface that is spin coated on silicone wafer and panel d) shows the topography of PS-air interface that is spin coated on freshly cleaved mica sheet. The roughness values are extracted on table (3.1). The dots with bright color on panel a, exists on silicone wafer that might be caused during manufacturing. Since the thickness of PMMA in our samples are above 100 nm, those particles is well covered by PMMA and it does not interfere with our experiments.

As explained, panel c and panel d, demonstrate the topography of PMMA-air and PS-air interface, respectively. One can detect a certain roughness and waviness on both of the interfaces. The values on the table (3.1) includes both of those patterns in the calculation of roughness values. However, comparing the height profile of one line on the image reveals that the waviness has an amplitude of almost two times larger than the small scale roughness. The waviness is typically on a more macroscopic length scale of $(3 - 4)\mu m$ and
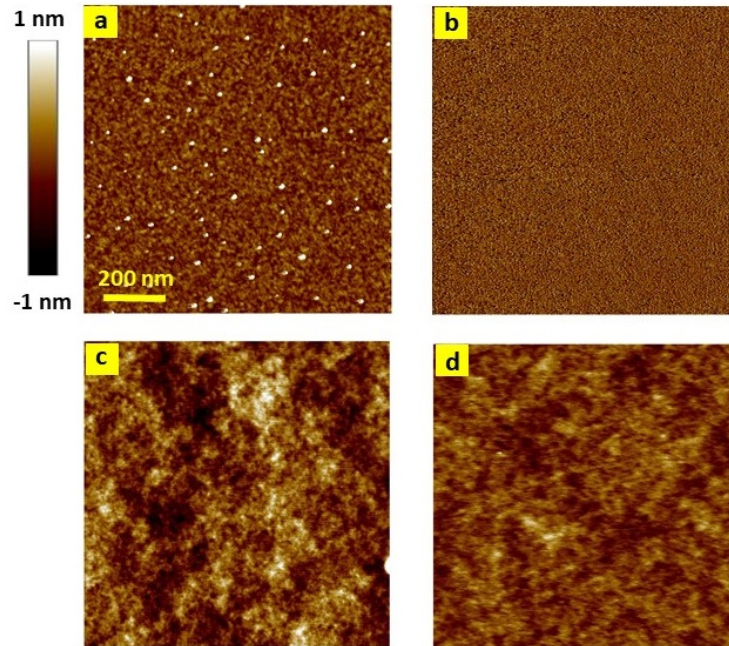
Figure 3.9: Topography of the interfaces, captured by AFM, soft tapping mode at room temperature. Panel a illustrates the topography of a Si/SiO-air interface, panel b, belongs to mica-air interface, panel c, regards to a PMMA-air interface on silicone substrate and panel d is the topography of a PS-air interface on mica substrate. The height scale is identical for all the images.

it seems to be caused by the thin film preparation process. Studies on the factors causing the waviness is not the purpose of this thesis and we continued experiments with the presence of the waviness on the interfaces. The details on the evolution of the waviness on the interfaces is described at section (4.7).

3.5   Glass transition temperature

The use of polymer in a temperature range depends on what properties are needed, since some properties of polymers are effected by temperature. for instance if the flexibility of polymer is important, the ability for the molecules to move as stresses are applied, is a key factor to attained. On that case, service temperature needs to be as high, where molecules are mobile. If the use of polymer requires a strong physical properties, the service temperature should provide polymer in the rigid, glassy state. This implies that the polymer has

high strength in such areas as compression and tension increase. In this section, a brief introduction on the structure of polymers and the factors involved in the property of polymers is explained.

Polymeric chains being very large are found in polymers in two forms, Lamellar crystalline form in which the chains fold and make lamellar structure arranged in regular manner and amorphous form in which the chains are in the irregular manner. The lamellar are embedded in the amorphous part and can communicate with other lamellar via tie molecules, see figure (3.10). Regarding the popularity of each form in a polymer bulk, Polymers may be amorphous or semi-crystalline in nature. Hence, the crystallinity is given by:

$$Crystallinity = \frac{\rho_c \left(\rho_s - \rho_a \right)}{\rho_s \left(\rho_c - \rho_a \right)} \times 100 \tag{3.3}$$

The ρ_c is the density of a completely crystalline polymer, ρ_a is the density of the completely amorphous polymer, ρ_s is the density of the sample. A typical range of crystallinity can be defined as amorphous (0) to highly crystalline (90%).

Polymers that have simple structural chains as linear chains by slow cooling rate will result in good crystallinity. Polymers having high degree of crystallinity are rigid and have high melting point, but their impact resistance is low. However, amorphous polymers are soft and have lower melting point. In addition, formation of molecules in amorphous part can be influence by the solvent, since solvent can penetrate the amorphous part easier than the crystalline part.

Polystyrene and polymethylmethacrylate are good examples of amorphous polymers, while polyethylene and PET polyester are good candidate for crystalline polymers. The semi-crystalline polymer shows both the transitions corresponding to their crystalline and amorphous regions. Thus, the semi-crystalline polymers have true melting temperatures (T_m) at which the ordered phase turns to disordered phase, whereas the amorphous regions soften over a temperature range known as the glass transition temperature (T_g). It should be noted that amorphous polymers do not possess melting point, but all polymers possess glass transition temperature. The polymer melting point (T_m) is increased if the double bonds, aromatic groups, bulky or large side groups are
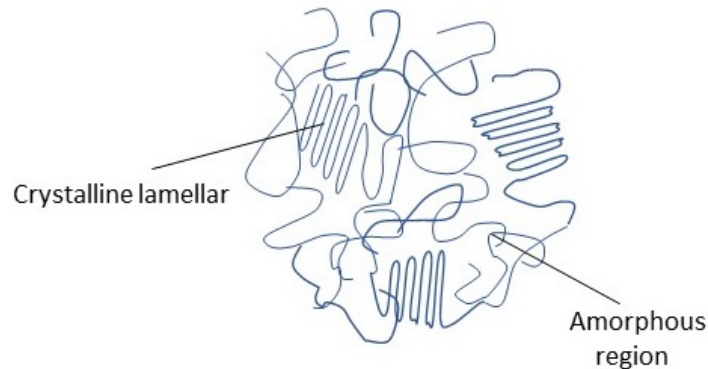
Figure 3.10: Sketch of the structure of a polymer, indicating the lamellar and amorphous regions.

present in the polymer chain, because they restrict the flexibility of the chain. The branching of chains causes the reduction of melting point, as defects are produced because of the branching. At low temperature the amorphous regions of a polymer are in the glassy state. In this state the molecules are frozen on place, they vibrate slightly but are not able to move significantly. The glassy state shows hard, rigid, and brittle nature comparable to a crystalline solid with molecular disorder. If the polymer is heated, it eventually will reach its glass transition temperature, the state where the polymer chains are able to wiggle around, and the polymer becomes soft and flexible similar to a rubber. This state is called the rubbery state. The temperature at which the glassy state makes a transition to rubbery state is called the glass transition temperature (T_g). Note that the glass transition occurs only in the amorphous region, and the crystalline region remains unaffected during the glass transition in the semi-crystalline polymer. The glass-transition temperature (T_g) of a material characterizes the range of temperatures over which this glass transition occurs. It is always lower than the melting temperature (T_m) of the crystalline state of the material, if one exists. In addition, at glass transition as the second order transition, the volume of the material does not change but the mechanical properties change drastically. while in melting point the volume changes.

The most important information that T_g provides is about the nature of the polymer at the temperature of use, whether it is rigid and glassy or it is flexible

and rubbery. Hard plastics like polystyrene and polymethylmethacrylate are used well below their glass transition temperatures, when they are in their glassy state. Rubber elastomers such as polyisoprene and polyisobutylene are used above their T_g, in the rubbery state, where they are soft and flexible [38].

The glass transition temperature depends on the mobility and flexibility (ease of the chain segment to rotate along the chain backbone) of the polymeric chains. If the polymeric chains can move easily, then the glassy state can be converted to the rubbery state at lower temperature. If somehow the mobility of the chains is restricted, then the glassy state is more stable and it is difficult to break the restriction causing the immobility of the polymer chains at the lower temperature because more energy is required to make the chains free. Thus, in this case, the glass transition temperature is raised. The glass transition temperature depends on factors such as intermolecular forces, molecular weights, etc. The more immobile the chain, the higher the value of T_g. For instance, the presence of bulky pendant group, such as a benzene ring, can restrict rotational freedom, leading to higher glass transition temperature. As in polystyrene, the presence of benzene ring increases the T_g. In polypropylene, there is no benzene ring leading to lower T_g value. The presence of flexible pendant groups, for example, aliphatic chains, limits the packing of the chains and hence increases the rotational motion, tending to deduce T_g value. In polybutylmethacrylate, the presence of large aliphatic chain reduces the T_g value when compared with that of polymethylmethacrylate. Plasticizers are low molecular weight and non-volatile materials added to polymers to increase their chain flexibility. They reduce the intermolecular cohesive forces between the polymer chains, which in turn decrease T_g. The glass transition temperature is also affected by the molecular weight of the polymer, T_g is increased with the molecular weight. The molecular weight is related to the glass transition temperature by the Fox–Flory Equation [39]:

$$T_g = T_g\left(\infty\right) - \frac{A}{M_n} \qquad (3.4)$$

where $T_g\left(\infty\right)$ is the value of T_g for very high molecular weights and A is the empirical parameter called Fox–Flory parameter related to the free volume

inside the polymer. It is observed that T_g is increased up to the molecular weight above a certain critical value, and after this limit, T_g is not affected considerably. The value of glass transition temperature might depend on the thickness of the polymer film. For instance, T_g values for PS film deviates from bulk values and it decreases with reducing the thickness of PS film [40]. This is an important remark in studying thin polymer films. Note, achieving certain property of polymer by increasing the heating temperature might cause the polymer to transfer from liquid state to melting point that in addition to mechanical properties, the other factors will change as well [41, 42].

3.6   Properties of polymers

Polymers such as polystyrene (PS) are very suitable model liquids to study the dewetting process, since they have a very low vapor pressure in the melt, so the mass conservation can be assumed. In addition, they are chemically inactive, non-polar, and their dynamics can be varied by choosing different chain lengths and annealing temperatures. For molecular weights below the entanglement length, the polymer melts can be treated as simple (Newtonian) liquid for the low shear rates in dewetting experiments [21]. Below the glass transition temperature T_g, the polymer films are glassy and experiments can be stopped in a certain stage and sample can be quenched to temperatures below T_g for further analysis. To conduct dewetting experiment, we select polystyrene and polymethylmetacrylate based on their optical properties to fulfill the condition for an unstable two layer polymer system that will be explained in more details later.

Polystyrene (PS) is an amorphous, nonpolar thermoplastic (figure 3.11, a). It is a very good electrical insulator, has excellent optical clarity due to the lack of crystallinity, and has good chemical resistance to diluted acids and bases. It is also easy to fabricate into a large number of finished goods since it is a viscous liquid above its glass transition temperature (T_g) that can be easily molded. The refractive index of PS is 1.5876 [29].
The PS chain length used in the experiments is $63\frac{kgr}{mol}$ with poly dispersity (qualification of distribution of chain lengths and molecular weights) of 1.03.

The bulk value for the glass transition temperature of PS $(63\frac{kg}{mol})$ is $100 \pm 5°C$ [43].
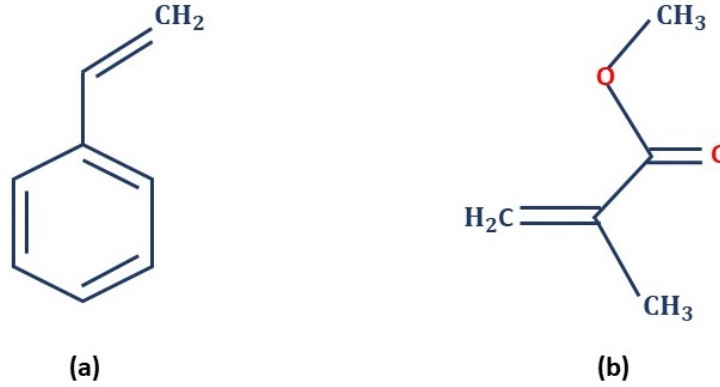

Figure 3.11: chemical structure of the monomers. a) shows the structure of PS monomer b) is the chemical structure of the PMMA monomer.

Another polymer, used for two layer polymer system is Polymethylmetacrylate (PMMA) with chain length of $10\frac{kgr}{mol}$. PMMA also known as acrylic glass, is a transparent, tough and rigid plastic (figure 3.11, b). Its properties remain stable when exposed to ultraviolet radiation and high pressure conditions. Therefore, it is an ideal substitute for glass. the refractive index of PMMA is 1.4889 [29]. the polydispersity $(\frac{M_w}{M_n})$ of the polymer we used for the experiments, is 1.05 and the glass transition temperature for bulk values is $97 \pm 2°C$ [44]. Both of the PS $(63\frac{kg}{mol})$ and PMMA $10\frac{kgr}{mol}$, were purchased from Polymer Standard Service Mainz (PSS-Mainz, Germany).

Viscosity of polymers in our experiments for the given chain lengths is controlled by variation of heating temperature. For this purpose for the various experimental runs, the imaging temperatures were in the range of $(120-130)°C$ to adapt the dynamics of the polymer system to the imaging speed of the AFM. The logarithm of PS viscosity in this temperature range varies between (6.99 ± 0.3) Pa.s and (5.99 ± 0.2) Pa.s and between (6.81 ± 0.1) Pa.s and (5.85 ± 0.3) Pa.s in case of PMMA (figure 3.12). The resulting viscosity ratio of PS and PMMA (for logarithmic values) thus is 1.02 for $T = 120°C$ and $T = 130°C$.
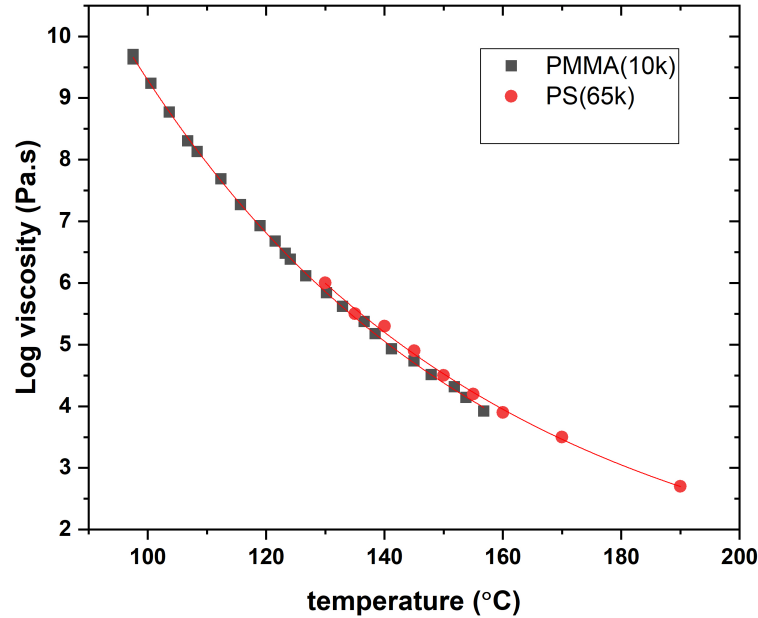
Figure 3.12: Viscosity of PS and PMMA as a function of temprature [45, 46]

3.7   Preparation of two layer polymer samples

Polymer films can be prepared by dip, spray and spin coating from. For this purpose, toluene is used as the solvent for both of the polymers. To achieve a homogeneous surface of the polymer film, we used static dispense spin coating technique where we set a droplet of polymer solution on the substrate and then start spin coating. Majority of solution is flung off the sides due to rotation of the stage and combination of centripetal force with the surface tension of the solution pulls the liquid coating into an even covering. The air flow dries the solvent, leaving behind just the polymer molecules on the substrate. The exact thickness of a film depends on the material concentration and solvent evaporation rate which depends on the viscosity of the solvent, The velocity of rotation, temperature and local humidity.

The layered polymer system was prepared on silicon wafer cuts of about (2×2) cm^2 having crystal orientation of $< 100 >$ and a natural oxide layer
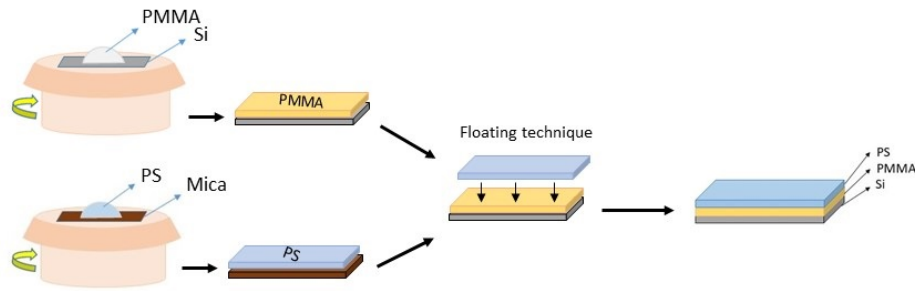
Figure 3.13: Sketch of preparation process for two layer polymer system, supported by silicon wafer. PMMA and PS are separately spin coated on silicone wafer and mica sheet, respectively, then using the floating technique, PS is transferred on top od the PMMA.

thickness of (2 ± 0.28) nm determined by ellipsometry (EP3, Accurion). Prior to coating, the silicon wafers were pre-cleaned with a fast CO_2 stream (Snow-Jet, Tectra) and then sonicated in ethanol, acetone and toluene. After each sonication step, the silicon wafers were blow dried with compressed nitrogen gas. As a last cleaning step, residual hydrocarbons were etched away by a 30 min dip in Piranha etch (fresh $50 : 50$ mixture of sulphuric acid and hydrogen peroxide (30%)) followed by a thorough rinse with hot ultrapure water. To prepare layered polymer films, first PMMA is spin coated from toluene solution onto such a pre cleaned wafer cut, the target PMMA film thicknesses for the experiments is either (111 ± 2) nm or (219 ± 2) nm. Second, PS was spin coated from toluene solution on freshly cleaved Mica sheets with thicknesses varying between about 2 nm and 10 nm suitable for experiments, floated on ultrapure water, and picked up from above with the PMMA coated silicon substrate, see figure (3.13). The thicknesses of the polymer films were determined by ellipsometry. In case of PMMA films this could be done using the thin film samples as described above. Since mica is optically biaxial material, it has several refractive indices and it makes precise optical measurements hard to achieve. Hence, to measure the thickness of PS films, we spin coated PS films on cleaned silicon wafers using the same solvent concentrations and spinning parameter as on Mica.

3.7.1   Removing PS

In the study of two layer polymer system, there is not any direct way to monitor the evolution of PS-PMMA interface, unless to remove the PS layer on top and monitor the PMMA-air interface. Most of the available chemicals such as acetone and toluene dissolve both of the polymers that damage the PMMA surface completely or partly during removing the PS. We use cyclohexane as the solvent to remove PS. It dissolves PS faster than PMMA and it has least damage on PMMA comparing to other accessible solvents. If the exposure time was long, it might cause damage and distort the structure on PMMA surface. Based on our observation, it takes less than 10 seconds for PS bulk to dissolve in cyclohexane that is annealed to $50°C$ that allows one to remarkably decrease the exposure time to the solvent and minimize the damage on PMMA surface. In this thesis, for PS with thickness in the range of $1-10$ nm, we tap the sample in cyclohexane of $50°C$ for 5 seconds and then dry it immediately with nitrogen jet.

4

Results and Discussions

4.1   Initial structure of the interfaces

Following the discussion at section (3.4) on the roughness of the polymer surfaces after spin coating, we would like to start this chapter with introducing the structure of the interfaces before conducting dewetting experiments.

Studying the topography of the polymer surfaces after spin coating, we notice one small scale roughness and another waviness at a larger scale on polymer surface. Figure (4.1, a) demonstrates the topography of a PMMA-air interface on silicone wafer after spin coating, captured by AFM. In order to compare the two described roughness, we plotted the height profile of one cross section (scan line) at panel b. The red line that is a smoothing function on the original data, shows the waviness. By excluding the waviness from the original data, the remaining structure can explain the small scale roughness. The (R_{rms}) value of the small scale roughness for PMMA-air interface is approximately 0.28 ± 0.03 (table 3.1) and the amplitude of waviness is approximately two times larger than the amplitude of the small roughness obtained by the height profile (panel b) of one cross section. The waviness is formed on PMMA-air interface with a characteristic wavelength around $1\mu m$ measured by power spectral density analysis (panel c), although this number might vary for different samples. Note that similar argument on the small scale roughness and large scale waviness is valid on a PS-air interface on mica sheet, see figure (4.2, b).
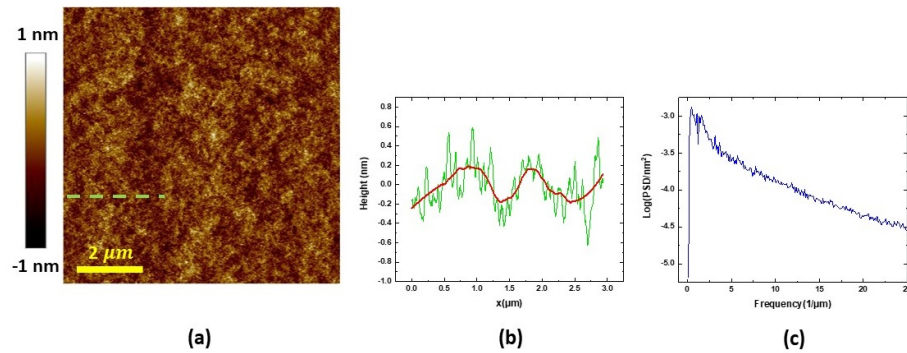
Figure 4.1: Topography and corresponding power spectral density analysis of a thick PMMA after spin coating on silicone wafer. Panel a, demonstrates the topography of a PMMA-air interface, Panel b shows the height profile of the dashed line on the image at panel a. Panel c, demonstrates the power spectral density analysis of the PMMA-air interface.

To study the structure of the final sample and compare it with the structure of the interfaces before transferring PS film on PMMA substrate, we mark a random spot on the PMMA surface after spin coating (figure 4.2, a) and then scann the same spot after transferring PS film (figure 4.2, c). Comparing the
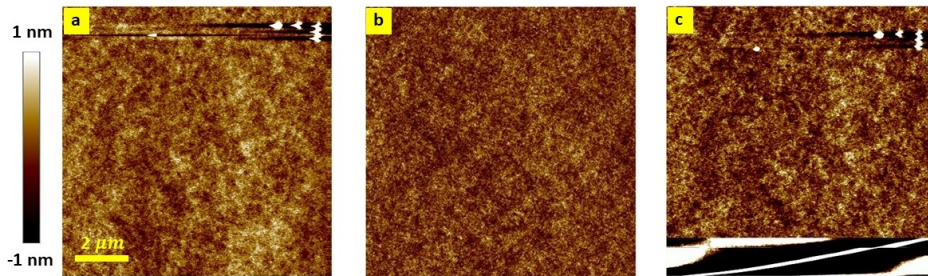
Figure 4.2: Topography of the interfaces involved in the final structures on the sample. Topography of PMMA-air interface after spin coating on silicone wafer (panel a), topography of PS-air interface after spin coating on mica sheet (panel b), topography of PS-air interface on the sample after transfer of PS film on top o the PMMA layer (panel c). The AFM marks are located on the top right corner of panel a and panel b.

two images (panel a and c), reveals a similar structure on the interfaces in large scale. The PS-air interface on mica sheet after spin coating (figure 4.2, b) is the interface that is transferred on top of the PMMA substrate and it has slightly smoother surface with roughness of approximately 0.17nm. In fact the structure of PMMA-air interface is traced by smoother and thinner PS

film and the waviness of the two polymers are locked into each other during transfer, creating a positive correlation of the interfaces.

4.2 Dewetting in two layer polymer films

As described at section (2.3), polymer films that are in unstable state of energy on a substrate, will minimize their energy with reaching the equilibrium state (see section 2.3). As predicted by the calculation of Hamaker constant and Van der Waals interactions in our experimental system, the upper layer spinodaly dewetts from the liquid under layer. In this system both of the polymers are in liquid state by annealing polymers above their glass transition, at a temperature where the viscosity of both of the polymers are equal. Such systems allow for richer dynamics compared to solid substrate and since the substrate is soft, the possible deformation and dynamics of lower layer can also be studied. In this thesis the experimental results is discussed and they will be compared with theoretical predictions.

To monitor the dewetting of one liquid from another liquid substrate, we used samples consisting of a nanometric thin PS film with molecular weight of $63\frac{kg}{mol}$ on top of an also nanometric film of PMMA with molecular weight of $10\frac{kg}{mol}$. The glass transition temperature of PS $(63k)$ is $T_{g,PS} = (95 \pm 5)°C$, while that of PMMA $(10k)$ is $T_{g,PMMA} = (115 \pm 5)°C$ [47]. Both polymers were purchased from Polymer Standard Service Mainz (PSS-Mainz, Germany) with polydispersities of $\frac{Mw}{Mn} = 1.03$ for PS and of $\frac{Mw}{Mn} = 1.05$ in the case of PMMA. The surface tension of the PS-air interface is $\sigma_{PS-air} = (32 \pm 2)\frac{mN}{m}$ that is about 25 times larger than that of the buried PS-PMMA interface $\sigma_{PS-PMMA} = (1.25 \pm 0.07)\frac{mN}{m}$ [47].

The dewetting process was monitored in situ by AFM in soft tapping mode. For the various experimental runs, the imaging temperatures were in the range of $(120 - 130)°C$ to adapt the dynamics of the system to the imaging speed of the AFM. The viscosity of PS in this temperature range varies between 9.8 MPa.s and 0.98 MPa.s and between 6.5 MPa.s and 0.71 Pa.s in case of PMMA [48, 49]. The resulting viscosity ratio between PS and PMMA varies accordingly

between 1.5 for $T = 120°C$ and 1.38 for $T = 130°C$ [47]. For some experiments the sample was quenched to room temperature at a desired dewetting stage and the frozen dewetting pattern at the PS-air interface could be imaged by AFM with great accuracy. Additionally, the PS layer could be removed by dipping it in a selective solvent (cyclohexane, Sigma Aldrich, Germany) for five seconds at $50°C$ and immediately blow drying with a gentle stream of nitrogen gas. Subsequently the formerly buried PS-PMMA interface could be imaged by AFM and potentially connected with the PS-air interface for a full three dimensional image.

Figure (4.3) shows the evolution of PS-air interface from a liquid PMMA substrate during dewetting process and you can follow the dewetting process from the step where the capillary waves amplifies (panel b) until PS layer dewetts into set of droplets (panel h).
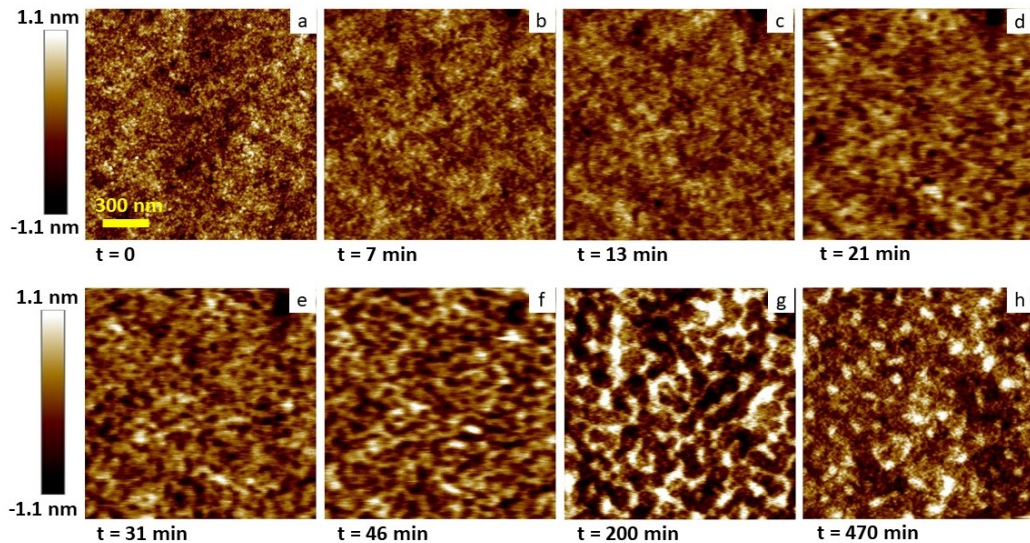
Figure 4.3: Evolution of PS-air interface captured in situ by AFM. A PS layer of 6 nm is transfered on top of a PMMA layer with thickness of 111nm. The heating temperature is $123°C$.

Figure (4.3, a) is the topography image of PS-air interface captured ex situ at room temperature where dewetting has not started. The R_{rms} roughness of PS-air interface on panel a, is 0.32 nm. On panel b, the capillary waves have been amplified and as the heating continues for longer time, dewetted holes

form on PS-air interface (panel c) and their radius grow with time. Panel f, illustrates the time step where growing holes meet the neighbor holes and start to coalescence. As you can see on panel g, as the heating continues further, the holes are not distinguished any longer, instead there are patches of PS that one see with lighter color. Later on those patches of PS shrink into strings, and then decays into droplets of PS on PMMA (panel h). The droplet in this stage are still developing and they are not yet in equilibrium state. After a proper time that depends on the viscosity of polymers, droplet will be equilibriated, having final equilibrium contact angle at three phase contact line. See [50] for the relaxation of larger droplets into equilibrium. The particular focus in this paper is the influence of the bottom, respectively of the PMMA thickness on the relaxation path. We conduct the experiments as described by annealing samples above the glass transition of polymers, monitoring the dewetting steps in situ by AFM. Then using the proper analyzing technique, we extract the data from AFM images. Further discussions and results on each step of dewetting on both of the interfaces, can be found at the following sections.

4.3   Amplification of capillary waves

Thermally induced height fluctuations, called capillary waves, that arise from the collective hydrodynamic motion of the liquid elements initiates perturbations on liquid surfaces [51]. When a bulk of liquid rises somewhere above the surface, the added volume of this parcel creates a pressure that is locally higher than normal, and this pressure pushes the fluid away from that place and piles it up a little further, generating another surface rise some distance away forming a repetitive pattern of disturbance. The capillary waves are harmonic waves with the surface tension acting as a restoring force and their presence has indirectly been verified by diffuse x-ray scattering and reflectivity measurements on the surface of various liquids [52]. It has been observed that the value of the measured roughness exceeds the intrinsic roughness caused by the liquid molecule size and hence yields an indirect proof of a height disturbance that makes the surface fuzzy. Initially, there would be a spread of wavelengths present and that some would grow while others would decay. The propagating

or damping of the wave depends on the wave vector, the surface tension, the dynamic viscosity, and the density of the liquid [53]. As film thicknesses approach molecular dimensions, intermolecular short-range and long-range forces lead to the amplification of destabilizing surface perturbations with the wavelength that is correlated to these forces in the form of capillary fluctuations. Since the driving force correlated to other wave length are absent, they will damp and will be suppressed by the stronger forces. The dominant driving forces greatly affect film dynamics and stability at the surface and interface of both simple and viscous polymeric liquids, such as spinodal dewetting and droplet coalescence [33].

The largest and smallest capillary wave vectors that are sustained by the interface, λ_{disp} and λ_{grav}, respectively, are determined by dispersion (or Van der Waals force, equation 4.1) and gravitational forces (equation 4.2).

$$\lambda_{disp} = \frac{2\pi\sigma_{lv}l^4}{A} \tag{4.1}$$

$$\lambda_{grav} = \frac{\Delta\rho g}{\sigma_{lv}} \tag{4.2}$$

The dispersive capillary wave vector λ_{disp} is a function of the surface tension σ_{lv}, the film thickness l and the Hamaker constant A for the interaction between the substrate and the air across the film. Wavelengths above this range are suppressed by gravitational forces and those below this range by dispersion forces. The average energy of each capillary wave is determined by the equipartition of energy. Equipartition of energy implies that molecules in thermal equilibrium have the same average energy associated with each independent degree of freedom of their motion. The energy per molecule is given by $\frac{1}{2}K_BT$, where K_B corresponds to the Boltzmann constant and T to the temperature. Integrating over the spectrum of capillary waves, the average mean square displacement of the interface $\langle\Delta\zeta^2\rangle$ is found as:

$$\langle\Delta\zeta^2\rangle = \frac{K_BT}{2\pi\sigma_{lv}}\ln\frac{\lambda_{disp}}{\lambda_{grav}}. \tag{4.3}$$

The amplification of capillary waves as a function of heating time is experimentally accessible in high viscous liquids that have slower dynamics. In the two

layers polymer system, observation of amplification of capillary waves (spinoda waves), leading to spinodal dewetting, is possible in principle. On the PS-air interface, we can scan a random area on the interface at room temperature and scanning continues on the same spot with annealing the sample to a certain temperature above glass transition temperature. The information on the amplitude of capillary waves is valid until the time step, when PS film breaks up and three phase contact line forms, later on both of the interfaces grow downward. Figure (4.4), demonstrates the topography of PS-air interface (panel a) with PS
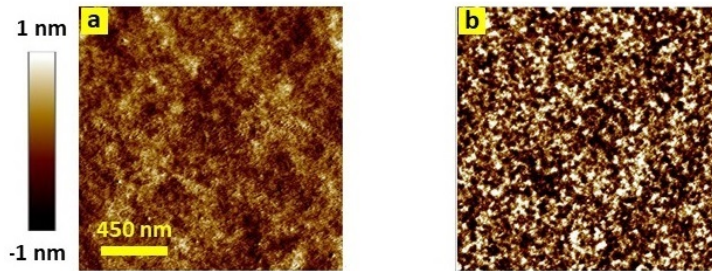
Figure 4.4: Topography of PS-air and PS-PMMA interface. The thickness of PS is 6 nm on top of a PMMA layer of 111 nm, heated for 4 min at temperature of 124°C. a) topography of PS-air interface, b) topography of PS-PMMA interface captured ex situ by AFM at room temperature.

of 6 nm on top of a PMMA layer of 111 nm that is heated for 4 min at 124°C. We stoped the heating and removed PS with a selective solvent (cyclohexane) and scanned the hidden PS-PMMA interface (panel b). As discussed both of the polymer layers in our system are liquid and we expect the growth of capillary waves on both of the liquid-air and liquid-liquid interfaces. However the annealing time of the sample at figure (4.4) is only 4 min, the amplitude of capillary waves in PS-PMMA interface is already developed and is clearly larger than the amplitude of spinodal waves at PS-air interface. In fact, on PS-air interface, the amplitude of spinodal waves are in the range of the roughness on PS-air interface and the surface tension of PS-air interface is way larger than the surface tension of PS-PMMA interface. Hence, based on the observation, the amplitude of capillary waves at PS-PMMA interface is larger comparing the amplitude of capillary waves at PS-air interface. In order to investigate further into the details, we analyze the interfaces by power spectral density. Figure (4.5), demonstrate the power spectral density and the corresponding
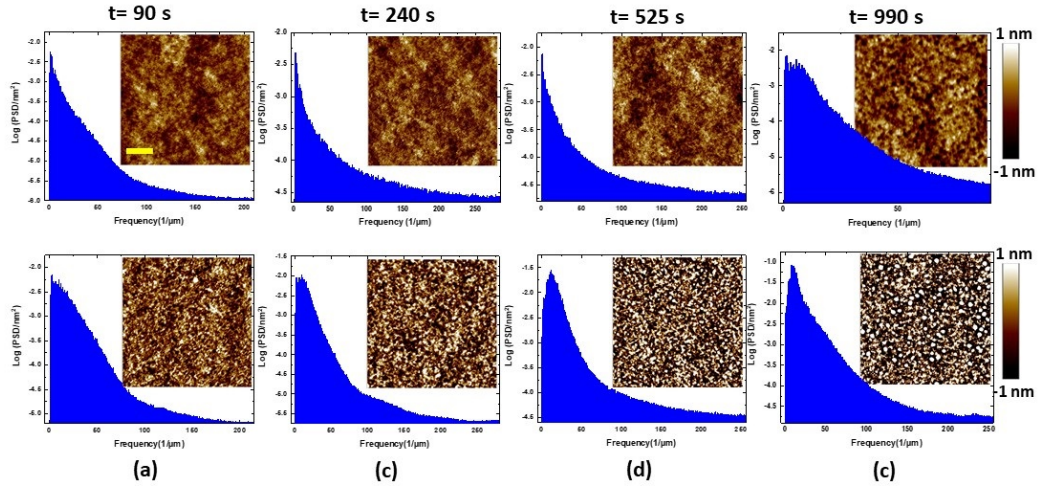
Figure 4.5: The power spectral density analysis of PS-air and PS-PMMA interface and corresponding topography image. Samples are heated at $124°C$ for different heating times of $90s$, $240s$, $525s$, $990s$ and scanned ex situ by AFM for both of the interfaces. The scale bar demonstrates 450 nm and the image on each column belongs to a same sample.

topography image of PS-air interface for several heating times (top row). As it can be seen, the power spectral density does not detect any clear peak before rupture time on PS-air interface, indicating the low amplitude of the spinodal waves, while we see clear signal of preferred wavelength on the PS-PMMA interface on the same samples (bottom row) from early stage of dewetting. Although the preferred wavelength on PS-air interface is detectable when few of holes have formed (panel d, top row). The reason for such observation is the maximum amplitude of spinodal waves on that stage. Since the amplification of spinodal waves at PS-air interface can not be monitored from early stage of dewetting, we lose the information on the dynamics of amplification. On the other hand, the clear peak on the power spectral density plot of PS-PMMA interface from early stage of dewetting indicates a clear signal of preferred wavelength, making this interface a good alternative to study the amplification of spinodal waves (see figure 4.5, bottom row).

To monitor the evolution of spinodal waves at PS-PMMA interface, we use four cuts of mother sample and we scan the corners that corresponds to the center of the mother sample on each of the cuts. This way we assure that

the scanning spots have the least thickness differences that might be cause by preparation process. Each cut is heated to different time scales, then the PS-air interface and PS-PMMA interface (after removal of PS) is scanned ex situ by AFM. The dynamics of growth of spinodal waves is analyzed until the rupture time and after that both of the interfaces grow downward and the amplitude of corrugations decrease.
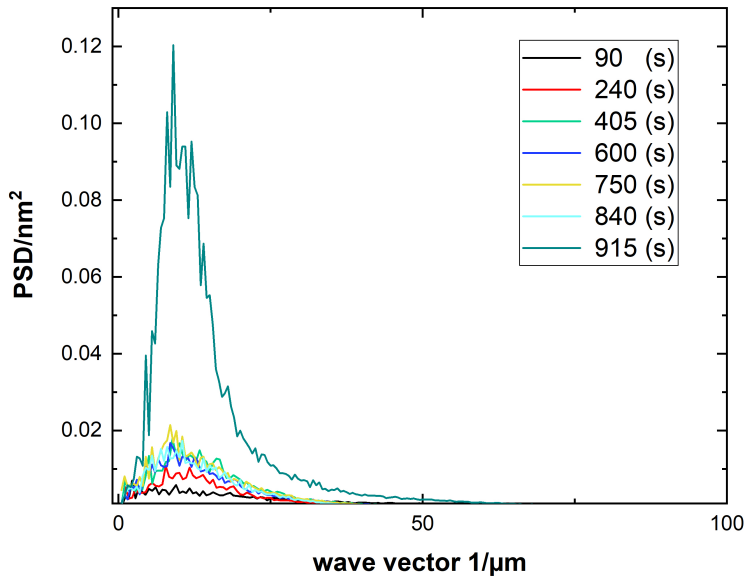

Figure 4.6: Power Spectral Density of PS-PMMA interface on different heating time indicates the selection of a certain wavelength in the order of approximately 100 nm that amplifies with heating time. Samples are prepared with PS layer of 6 nm on top of a PMMA layer with thickness of 111 nm. The annealing temperature is $124°C$.

Figure (4.6), shows power spectral density of the and PS-PMMA. The graph demonstrates the growth of a certain wavelength in the range of approximately 100 nm with heating time. Spinodal waves continue to grow in amplitude until the three phase contact lines form on PS-air interface. The wavelength is constant during the amplification, indicating the selection of a certain wavelength in accordance with the driving Van der Waals forces that grows the fastest. We can quantify the amplitude of spinodal waves as a function of heating time using the power of the peaks in power spectral density analysis from figures such as (4.6). Figure (4.7) demonstrates the amplification of spinodal wavelength on
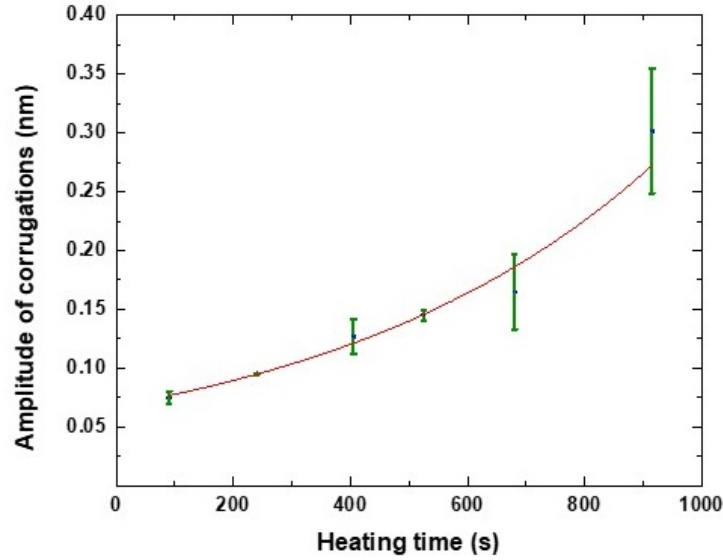
Figure 4.7: Amplification of spinodal wavelength of approximately 100 nm on PS-PMMA interface obtained from power of the Power Spectral Density for PS of thickness 6 nm on PMMA layer of 111 nm for several samples. The experiments are conducted at temperature of $124°C$

PS-PMMA interface as a function of heating time. The values are the average value extracted from the power spectral density analysis of several samples. The red line presents an exponential fit to the experimental data, indicating the exponential growth of capillary waves.

4.4 Rupture time

As discussed, the PS film on PMMA film dewets from the substrate by forming holes that eventually lead to the set of dewetted PS droplets on PMMA substrate with a certain contact angle. In this section we will discuss the topography change on PS-air interface during rupture and also the time scale it takes for PS film to break up into holes. We mention this time scale as rupture time τ.

Since holes need to grow to considerably large size to be optically visible, we use AFM to measure rupture time in early stage of hole formations by scanning a random spot on PS-air interface. Hence, we need to recognize the spots that presents the formation of three phase contact line, at first.
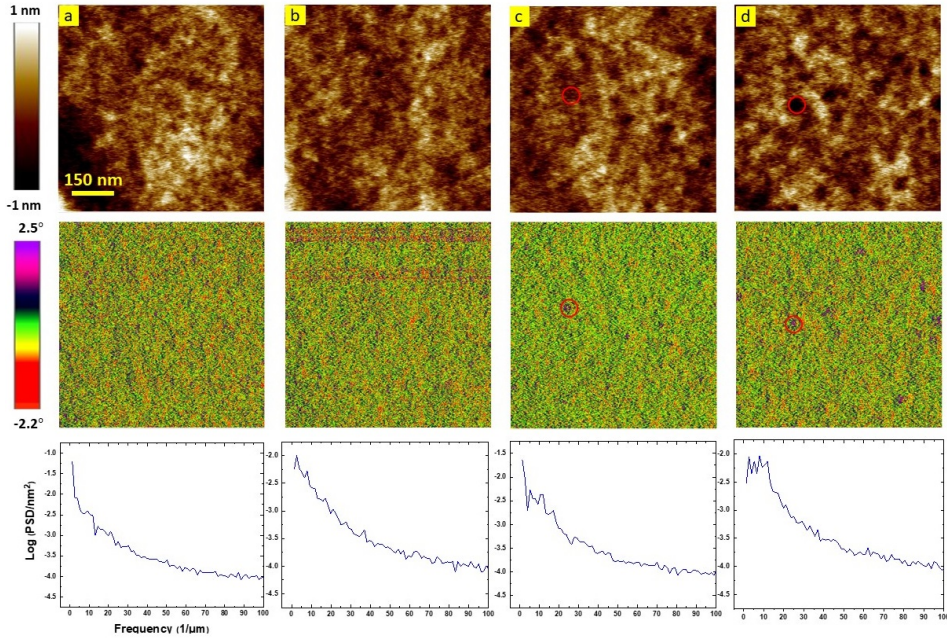
Figure 4.8: Dewetting process leading to the formation of three phase contact line. Panels a,b,c,d demonstrate the time steps of 25, 38, 71, and 97 minutes of annealing the sample and belong to the same spot on PS-air interface with PS thickness of 6 nm on a PMMA layer with thickness of 111 nm. The first row demonstrate the topography image and second and bottom rows show the corresponding phase signal and power spectral density analysis. The images are captured in situ by AFM, at temprature of 120°C.

Figure (4.8), demonstrates the break up process of a PS film. Panel a, b, c, d demonstrate the topography images (top row) and phase signals (second row) of the PS-air interface. The images demonstrates the evolution of PS-air interface with time and belong to a sample with PS layer with thickness of 6 nm on a 111 nm PMMA layer. We captured time steps of $25, 38, 71, 97$ minutes after annealing the sample to 120°C in situ by AFM. The bottom row of the figure (4.8) demonstrates the power spectral density of the corresponding topography images. As one see on panel c, after 71 minutes of heating, the first hole is formed that is marked by a red circle on topography image and also on corresponding phase signal (section 3.1). The different interaction of AFM tip when approaching materials with different properties is qualitatively reflected as color contrast on phase signal and here the PMMA is detectable on the middle of the red circle by purple color, indicating the formation of three phase contact line. In addition, the power spectral density analysis, illustrates a peak

presenting a wavelength of around 100 nm known as the spinodal wavelength.
If annealing the polymers continues, more holes will form (panel d). Based
on the round geometry of the holes and studying the material contrast on the
exact spot, we can confirm that holes are in fact formed at the most pronounced
depressions of the PS-air interface. However, due to slight differences in depth
of the depressions and the corresponding rupture time and fast expansion of
formed holes, not every local depressions will lead to the formation of a hole.
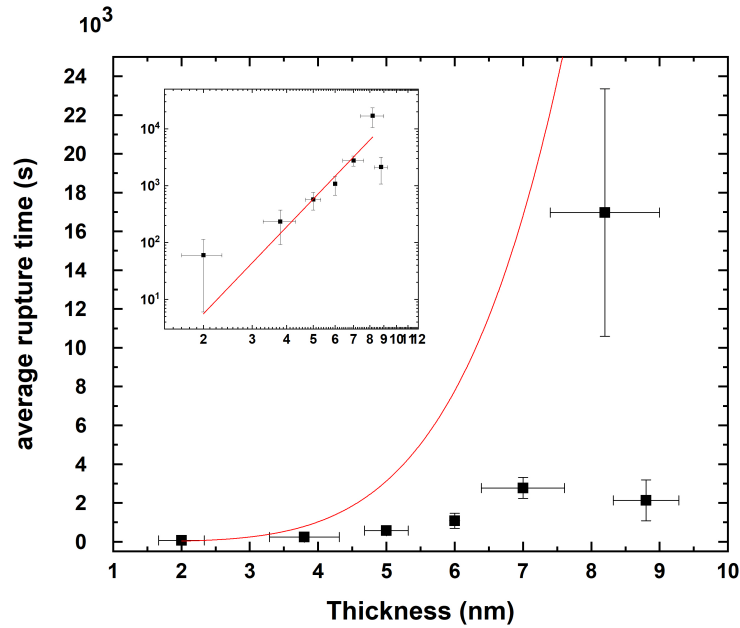
Figure 4.9: Rupture time for various PS thickness on PMMA layer of 111 nm at the
temperature of $125°C$. The black squares demonstrate the experimental data and the
green line the theoretical prediction. The red line in the inset graph demonstrates a
linear fit on the logarithm of the experimental data.

The rupture time depends on the strength of the driving forces and viscosity
of polymers and consequently on the annealing temperature. The dewetting
velocity for thin PS films at temperature of $125°C$ is very high that is experimen-
tally inaccessible to monitor the evolution of PS-air interface in situ by AFM
and to capture the rupture time. Thus, we re-scale the rupture time obtained at
different temperatures respectively polymer viscosities to the polymer viscosity
at $125°C$ using the following relation:

$$\tau_{125°C} = \frac{\nu_{125°C}}{\nu_{exp.temp}} . \tau_{exp.temp} \tag{4.4}$$

that ν is the viscosity and τ is the rupture time of the PS at the given temperature. Figure (4.9), demonstrates the rupture time for PS films with various thicknesses on PMMA layer of 111 nm. As discussed, the holes don't form at the same time, thus the rupture time depends on local details. More ever it is measured in situ by AFM and constantly scanning one spot manipulates the dynamics of evolution of the interface and correspondingly the rupture time has a fairly large experimental uncertainty. Slope of the linear fit on logarithm of the data on inset graph, indicates the growth of rupture time with fifth power of PS thickness that is compatible with experimental findings of PS layer on silicone substrate [19].

4.5 Spinodal wavelength

In this section, the spinodal wavelength before break up and holes distance after break up is discussed. We argue whether the preferred holes distance is equal to spinodal wavelength indicating the amplification of spinodal waves leading to the rupture of the PS film and also we will discus the effect of thickness of both of polymer films on the spinodal wavelength.

As it already discussed in section (4.3), the spinodal corrugations get amplified and reach their maximum amplitude at rupture time and at this moment, the two interfaces meet and the PS film ruptures forming three phase contact line. Since we face difficulties monitoring the spinodal waves before rupture time due to the roughness on the PS-air interface, we rely on the measurements at rupture time when the amplitude of the preferred wavelength grew to the same order as the amplitude of the initial surface roughness.

Figure (4.10), demonstrates the evolution of PS-air interface and corresponding power spectral density analysis before rupture time (panel a), at rupture time (panel b) and after rupture time when the holes density grow (panel c). The spinodal wavelength that is recognized by location of the peak on the power spectral density plot is distinguishable on all of the plots on figure (4.10) around
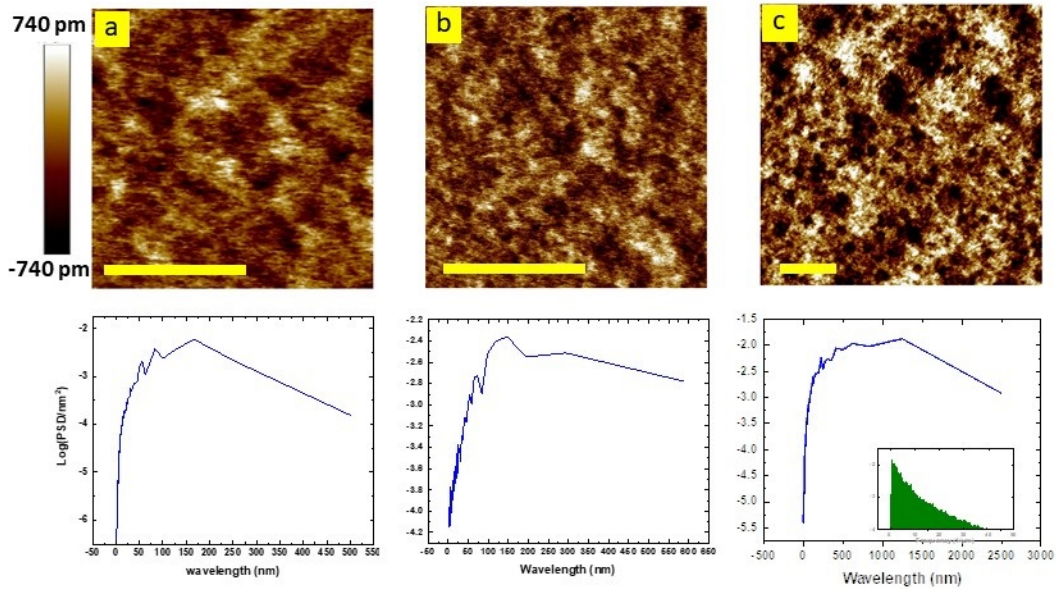
Figure 4.10: Time series of a 7 nm PS film dewetting on top of a 111 nm PMMA. Column a, shows the situation for an annealing time of 4 min and Column b, for an annealing time of 20 min captured in situ by AFM at temperature of $128°C$ and column c on the same sample heated for 38 minutes at $128°C$. Image c, was recorded ex situ at room temperature and shows a larger scan area. The topographic images are shown in the first row and the corresponding surface analysis by power spectral density are shown in the bottom row. The scale bar on the images correspond to 250 nm on the sample.

120 nm, although it is more pronounced on panel b that the corrugations have the largest amplitudes. The exact value of the spinodal wavelength obtained by power spectral density analysis for the sample presented at figure (4.10) is 120 ± 20 nm that the error is from single sample measurement caused by dislocating the peak and consequently the sharper the peak the smaller the error. The data indicates the selection of a certain wavelength that grows steady with time and achieve its maximum amplitude short moment before rupture time and the same wavelength leads to the rupture of PS film and formation of holes. Comparing panel b and panel c, we see that the power spectral density analysis is valid after the rupture time, where holes are in the early stage and have not been formed pronounced rims. Note that using the power spectral density analysis still provides good results after rupture time. Even though the Power Spectral Density analysis before and after rupture time indicates

that the growth of capillary waves are the cause for dewetting, we would like to apply another analysis to avoid any possible error caused by the growth of rims around the holes in the power spectral density analysis. Therefore we benefit from the pair correlation function analysis on the image at panel c to compare the result of the two analysis on preferred holes distance. The
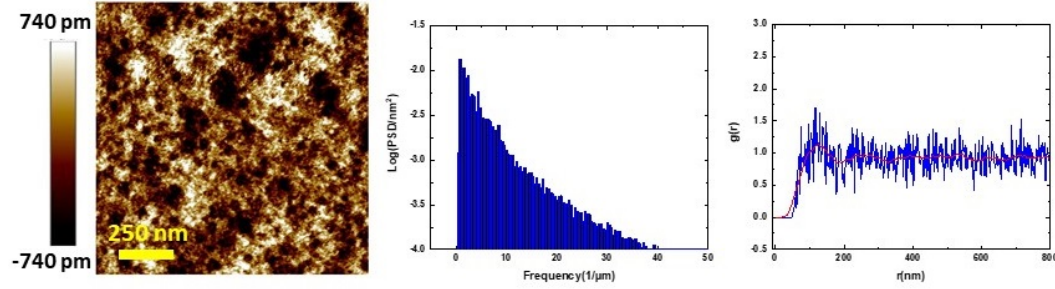

Figure 4.11: Topography of PS/air interface of a 7 nm PS on top of a 111 nm PMMA after three phase contact line has formed and associated power spectral density and pair correlation function analysis fitted with an smoothing function for clarity (red line).

two-point correlation function g(r) of the point set obtained at the position of the center of the holes is plotted in figure (4.11). The plot indicates domination of a certain holes distance in the range of (122 ± 5) nm. The value of preferred wave length obtained by power spectral density function before film ruptures $(120 \pm 20$ nm$)$ and the preferred hole distance analyzed by pair correlation function after hole formation indicates that both values agree closely within experimental error. Based on these results we can confirm that holes are in fact formed at the most pronounced depressions of the PS-air interface caused by the amplification of capillary waves. Note that power spectral density analysis is not reliable for the interfaces with developed holes. Figure (4.12) demonstrates the topography of a 9 nm PS film in our system. The rupture of the PS film in caused by heterogeneous nucleation (section 2.3). The power spectral density analysis is not a reliable method to measure the holes distance, since the holes are well developed and have formed rims and the analysis might measure the distance between the two close rim instead of the distance between the center of the two holes. Hence, for such cases pair correlation function analysis in the proper method to compute the holes distance, see panel b. As one see from

panel b, for that thickness of PS (9 nm), the preferred holes distance is not detected by the analysis and rupture is due to heterogeneous nucleation.

**(a)**   **(b)**
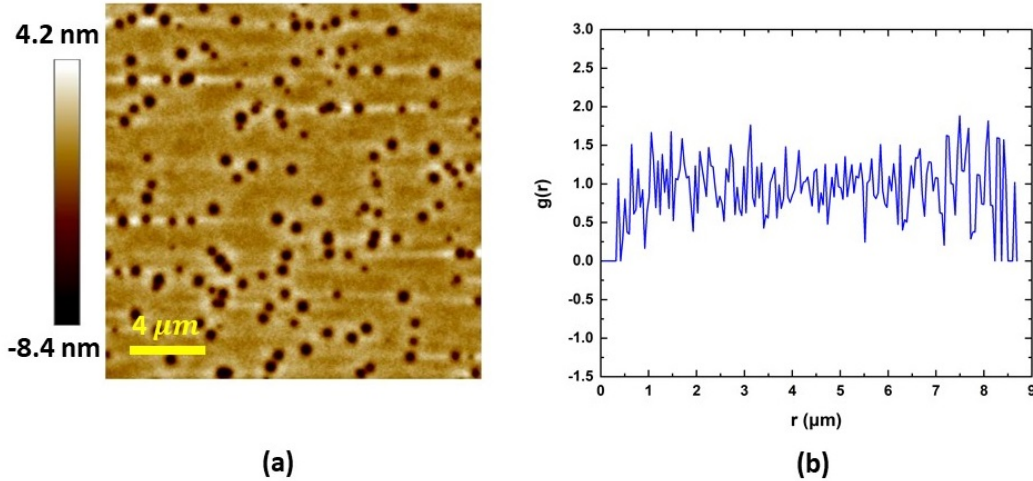
Figure 4.12: Topography of dewetted PS with thickness of 9 nm on a PMMA layer of 111 nm and corresponding pair correlation function analysis.

As expected for a spinodaly unstable film system, thickness of polymers affects the magnitude of Van der Waals forces and consequently on the value of spinodal wavelength. Figure (4.13), shows the experimentally observed spinodal wavelength λ_s for PS films with thickness in the range of $(2-9)$ nm emerging on PMMA films with thicknesses of 111 nm (blue squares) and 219 nm (red triangles), respectively. The data points indicate an increasing wavelength for increasing PS film thickness. The experimentally accessible thickness range is limited to lower PS film thickness by the inability to preparation thinner PS films. Whereas, for PS films thicker than about 9 nm a spinodal wavelength could not be detected reliably. The likely reason for that is that the driving Van der Waals forces weaken for increasing film thickness leading to long rupture times and thus any other nucleation eventually cause dewetting (figure 4.12). However for thickness of 9 nm, the wavelength is determined also by the pattern between the holes by power spectral density analysis. The preferred wavelength for each individual PS film thickness is independent of the thickness of the underlying PMMA layer for the two tested PMMA thicknesses that implies insensitive interactions in terms of intermolecular forces between silicone wafer or silicone dioxide with PS through PMMA layer. This justifies the initial made
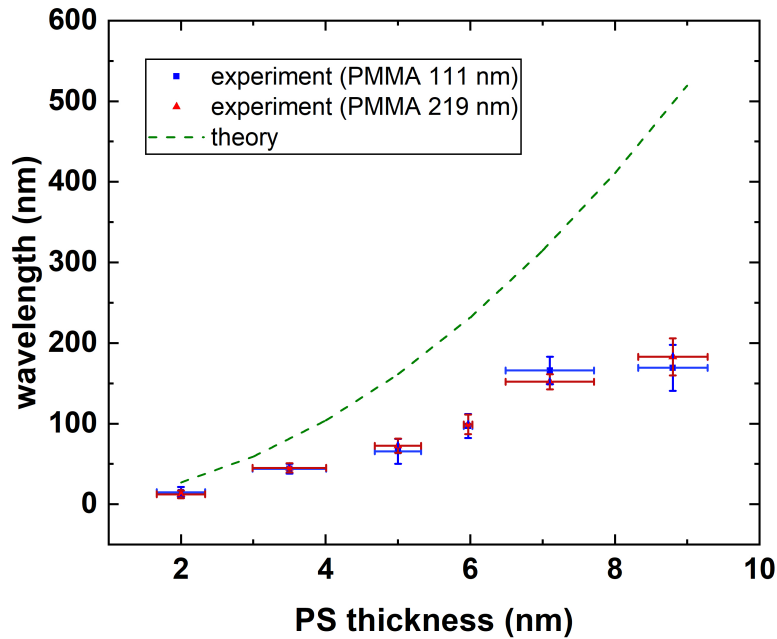
Figure 4.13: Spinodal wavelength of PS with variable film thickness on PMMA having a film thickness of 111 nm (blue squares) and 219 nm (red triangle) as determined by power spectral densities of the respective surfaces. The dashed green line presents the theoretical predictions for spinodal wavelength on a 111 nm PMMA film.

choice of using PMMA film thicknesses above 100 nm. The theoretical prediction, computed based on linear stability analysis is demonstrated by dashed green line. There is a remarkable deviation between the experimental and theoretical results. The reason for that is in theoretical simulations, the initial interfaces is considered to be flat, while in reality there are larger structures on the interfaces that is caused by preparation process (section 4.1) and it has remarkable impact on the mode selection and so the preferred wavelength [54]. In addition, uncertainty and error in computation of the parameters such as surface tension, viscosity and Hamaker constant is another reason for the deviation of results.

Based on the discussions we made at the sections above on rupture time and preferred wavelength as a function of PS thickness, we can safely mark the dewetting in our two layer polymer system as Spinodal dewetting.

4.6   Deflection of the interfaces

Although Young's equation is useful to explain wetting phenomena in nature, it only accounts for the in-plane balance of the three interfacial tensions near the three-phase contact line. The vertical component of the liquid surface tension, $\sigma_{LV} \sin \theta_{eq}$, remains unbalanced and results in a vertical net force applied on the substrate. Moreover, the Laplace pressure ΔP, which is inversely proportional to the droplet curvature $\Delta P \approx \dfrac{\sigma_{LV}}{R}$ is exerted to the liquid-solid interface. Considering a situation where the surface tension forces are stronger than gravity force, the liquid will be pulled into the vapor phase forming consequently, a so-called wetting ridge near the three phase contact line, see figure (4.14, b). For rigid solids like silicon and steel, the wetting ridge is of molecular scale and its influence on the contact angle can safely be ignored (figure 4.14, a). In contrast, for soft solids such as biological tissues and polymer gels or liquids, it can be up to sub-millimeter scale and thus it can strongly affect the wettability [55]. In the static case of a sessile droplet deposited on a soft substrate, the substrate deformation leads to a rebalancing of the interfacial tensions and to a modification of the contact angle, described by the so-called Neuman's triangle. The strength of normal component of surface tension combined with Laplace pressure defines the magnitude of the Neuman contact angle. Hence, it would vary with the droplet of different sizes [50]. Figure (4.14, a) schematically shows the surface tension forces on a solid substrate, while figure (4.14, b) shows in case of a soft substrate.

In case of dewetting on a soft substrates, the liquid-liquid interface is no
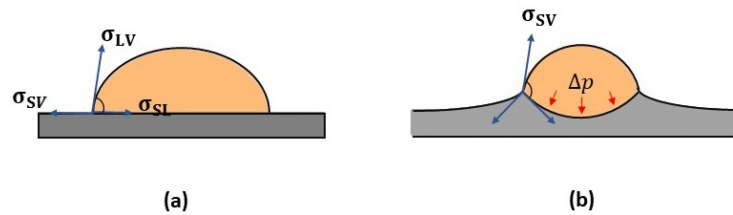
Figure 4.14: Liquid droplet on rigid and soft substrate. a) liquid droplet on solid substrate that he contact angle is defined by Young's equation. b) liquid droplet on soft substrate that the contact angle is defined as Neuman triangle.

longer constrained to a plane and any change on the topography of upper layer

will be imprinted on the lower layer. In case of spinodal dewetting in two layer polymer system of our interest, the capillary waves will be amplified on both of the PS-air and PS-PMMA interfaces and as the surface tension of the PS-PMMA interface $\sigma_{PS-PMMA} = (1.25 \pm 0.07)\dfrac{mN}{m}$ is about 25 times lower than the PS-air interfacial tension $\sigma_{PS-air} = (32 \pm 2)\dfrac{mN}{m}$, the buried PS-PMMA interface is even expected to have a significantly larger amplitude than the PS-air interface [16]. The latter is confirmed by our experimental observations, see figure (4.15), showing that the preferred wavelengths for both of the PS-air and the PS-PMMA interfaces are equal obtained by power spectral density analysis. The amplitude of the preferred wavelength obtained by the power of the power spectral density analysis is four times larger (in average) for the PS-PMMA interface with respect to that of the PS-air surface, short time before three phase contact line forms.

Knowing that the same wavelength develops both at the free and the buried
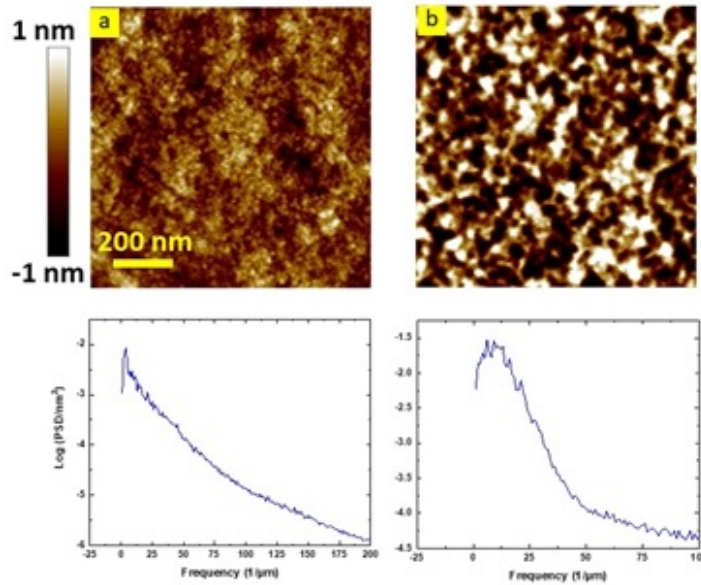
Figure 4.15: Topography of a 6 nm PS film on a 111 nm PMMA film, annealed for 14 minutes at 124°C. Panel a, Showing the PS-air interface and panel b, the associated PS-PMMA interface after removal of the PS with a selective solvent. The preferred wavelength for both of the interfaces is approximately 105 nm according to power spectral density in bottom row. (the second peak on the PSD of panel a is 26 nm that is in the order of diameter of round structure, the future holes, on the images).
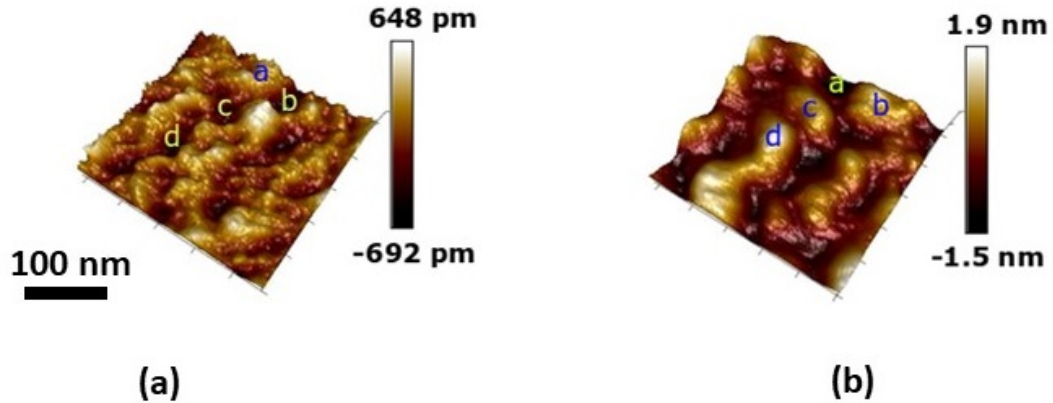
Figure 4.16: Deflection of the PS-air interface (panel a) and of the PS-PMMA interface (panel b) after removing the PS layer. Both of the images are captured ex situ by AFM at room temperature. The film thickness of PS is 6 nm and that of the PMMA layer is 111 nm. Scan area is 250 nm in 250 nm.

interface the question remains if these correlations are in-phase or antiphase, as theoretically predicted to be antiphase[34]. To experimentally study the deformation of interfaces, we scan a random area in situ by AFM and stop annealing the sample the shortest time before rupture time. Note that both of the interfaces will grow downward after rupture time and analyzing the correlation of interfaces after rupture time, could end in wrong conclusion. Thus after quenching the sample to room temperature, a random area on the PS-air interface is marked by AFM tip, then we scan by AFM (figure 4.16, a). To study the deformation on PS-PMMA interface, we remove PS with selective solvent and find the exact same spot using identifying marks made by AFM and then scan it (figure 4.16, b). Note that the height scale of the PS-air interface is about 2.5 times smaller than that of the PS-PMMA interface and the molecular roughness of the interface is much more visible. To make the comparison between the corrugations of the PS-air and the PS-PMMA interface easier some corresponding spots were marked with letters (a - d). This comparison reveals that raised parts in panel a, correspond to lowered parts in panel b, and indicates that the corrugations of the PS-air and of the PS-PMMA interface are antiphase. It is also clearly seen that the amplitude of the corrugation in panel b (PS-PMMA interface) is clearly larger than that at panel a (PS-air interface).

4.6.1 Overlapping the topography signal and phase signal

However, a precise correlation of both interfaces is difficult due to the small amplitude of spinodal wavelength at the PS-air interface and the corresponding masking by large scaled roughness of the PS-air and PS-PMMA interfaces that originate from the preparation process (section 3.4). Thus we used an alternative approach by additionally recording the phase signal during in situ AFM scanning at elevated temperature. The relative shift of the phase signal indicates a local variation of the imaged material based on the different interaction of AFM tip with materials with different properties. Thus when a hole forms and the underlying interface come into touch with AFM tip, the phase signal unravels where the holes form. Figure (4.17), shows two subsequently recorded AFM images in a stage where holes are being formed. To make the hole formation process clearly visible the topography is displayed in a three dimensional rendering while the color code of the skin encodes the phase signal. The spot marked in the topography image, figure (4.17), illustrates for example a valley in the deflected PS-air interface, whereas the dark blue color indicates that the surface material is PS. Imaging the same spot about 3 min later, the amplitude of the topography increased slightly while the phase contrast became much clearer. In particular the marked spot in panel b shows now a phase signal corresponding to PMMA (light blue). This shows that the PS film ruptures in the valleys, indicating an anti phase deflection of the interfaces [16].

4.7 Evolution of the large wavelength

As discussed at section (4.1), the large scale waviness is initiated at the PMMA-air interface during preparation process and the structure is followed by PS film during transfer, creating a positive correlation of the waviness on the interfaces. In this section we discuss the wavelength associated with the waviness (large wavelength) and its evolution during the dewetting process.

Figure (4.18) demonstrates the topography of each of the interfaces before and after dewetting experiments on the same spot and the corresponding
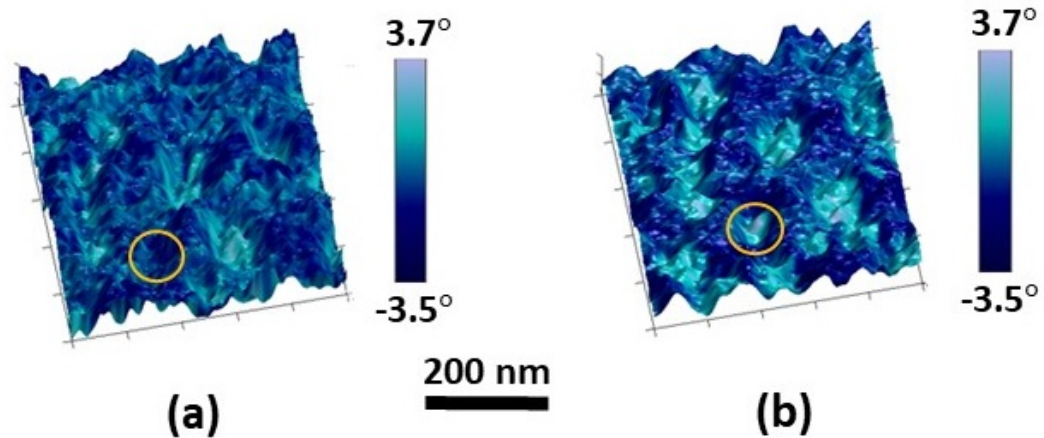
Figure 4.17: AFM images, combination of height and phase signal, showing the temporal PS-air interface evolution of a 6 nm thick PS film on a 111 nm thick PMMA film in a scan area of 430 nm in 430 nm. The time difference between the consecutive images is 184 (s) captured in situ at 127°C.
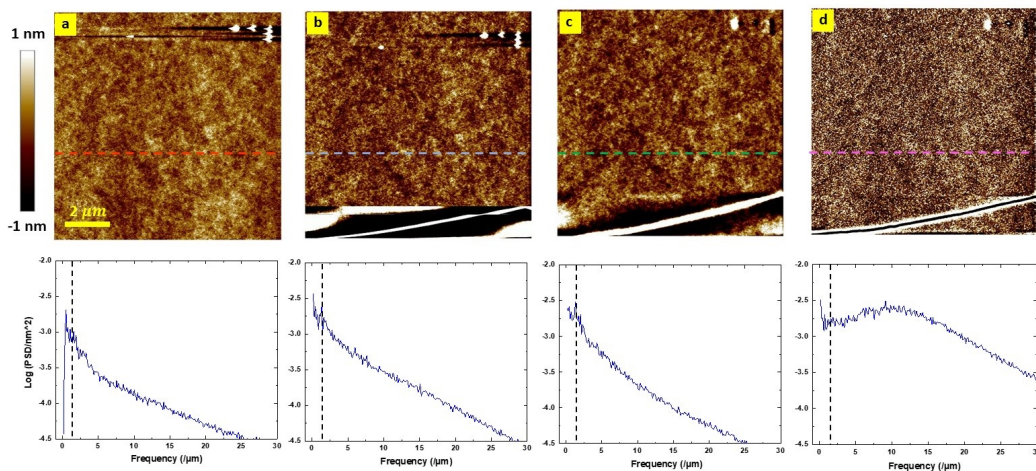

Figure 4.18: Topography of the interfaces before and after conducting the dewetting experiment and corresponding power spectral density analysis. Panel a demonstrate the topography of PMMA-air interface after preparation, panel b, the topography of PS-air interface after transfer on top of the PMMA layer, panel c, the topography of PS-air interface after dewetting and panel d, the topograpgy of PS-PMMA interface after dewetting and after removal of PS. Sample consists of a PS layer of 7 nm on top of a PMMA layer of 111 nm and the dewetting conducted at temperature of 125°C for 8 min. The power spectral density analysis is applied to the cropped image of 6μm size in order to exclude the defects from images. The location of peaks in each of the plots is marked by perpendicular line on each of the plots.

power spectral density analysis. Panel a, demonstrates the PMMA-air interface after spin coating and panel b, shows the topography of PS-air interface after transferring the PS film on top of the PMMA layer and before conducting the dewetting experiment. We conduct the dewetting experiment at temperature of $125°C$ for 8 min and scan the same spot on PS-air interface (panel c), then we remove the PS and scan the same spot on PS-PMMA interface (panel d). As one read from the power spectral density analysis, the large wavelength in the range of approximately (700 nm) is detected on this sample and it is formed on the two interfaces before and after dewetting. We expect the growth of spinodal wavelength after dewetting and since the surface tension of PS-air interface is approximately 25 times larger than the surface tension of PS-PMMA interface and as it discussed at section (4.3), the spinodal wavelength can not be clearly detected on this interface (see panel c) making the large wavelength the dominating wavelength in the power spectral density analysis. Although, the power spectral density analysis of PS-PMMA interface after dewetting (panel d) shows two clear peaks, one belongs to large wavelength and the second peak that corresponds to spinodal wavelength. Comparing panel b and panel c shows that the amplitude of large wavelength does not vary considerably while comparing the panel a and panel d indicates growth of around two times for large wavelength using the value of the power of power spectral density.

To simplify the comparison, we would like to continue the discussion based on the height profile of one scan line. Figure (4.19) shows the height profile of the lines marked on each of the topography images at figure (4.18). All the heights are plotted on one graph and to make the comparison easier we moved each of the plots vertically on top of each other, as a result the value on y axis are not global height scale. The red and blue line belongs to the PMMA-air interface after spin coating and PS-air interface after transferring on PMMA, respectively, where the green line and pink line belongs to PS-PMMA and PS-air interfaces after dewetting, respectively. As we see the higher surface tension of PS-air interface does not allow for considerable change for this interface at this stage of dewetting, while the PS-PMMA interface is developed considerably and spinodal corrugations are clearly visible. The amplified spinodal corrugations make the pattern of the large wavelength barley visible that explains the weaker signal on the power spectral density plot of panel d at figure 4.18. Although
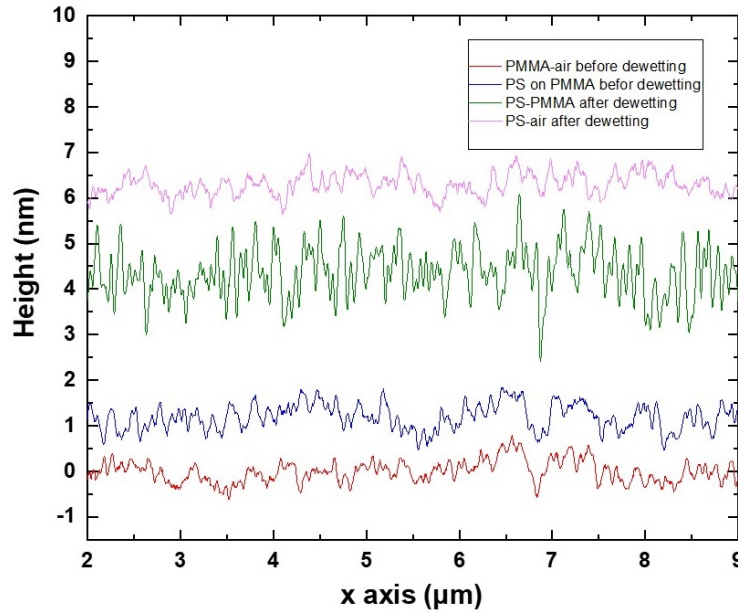
Figure 4.19: Height profile of one line at same spot, marked on each of the images at figure (4.18. The red line corresponds to PMMA-air interface after spin coating on silicone wafer, the blue line corresponds to PS-air interface after transfer of PS on top of the PMMA layer, the green line corresponds to PS-PMMA interface after dewetting and after removal of PS, and the pink line corresponds to PS-air interface after dewetting.)

the correlation of the interfaces in case of large waviness remains positive to this stage of dewetting.

To study the possible change in the correlation of large wavelength, we continue the dewetting experiment on the similar sample up to rupture time, where few of the holes have just formed.

Figure (4.20) demonstrates the topography of PS-air (panel a) and PS-PMMA (panel b) interface after conducting the dewetting experiment on the same spot. Comparing the topography of interfaces reveals the positive correlation of large wavelength, meaning that the correlation of large wavelength remains positive until the rupture time. We can have a look on the topography of interfaces in more details by selecting a random line on both of the interfaces on the same spot, and we transfer the profile of those line on top of each other (see 4.20, c). However the PS-PMMA interface is developed and the amplitude of spinodal corrugations are shading the signal from large wavelength.
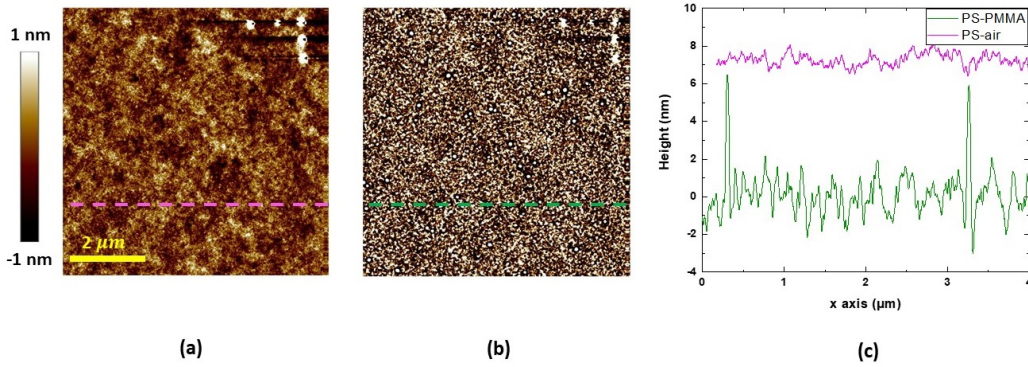
Figure 4.20: Topography of PS-air interface (panel a), PS-PMMA interface (panel b) and the height profile of the marked lines (panel c). The PS layer of 7 nm on top of a 111 nm PMMA layer, heated at 128°C for 16 min.

The clear message we get from the discussions above is the confirmation of positively correlation of large wavelength until rupture time. The evolution of the interfaces and the dynamics of existing wavelengths after rupture time is discussed at the following section.

4.8   Amplification of a secondary wavelength after rupture time

We discussed the spinodal wavelength in our two layer polymer system at section (4.2) and with enlarging the scan area, we also covered the discussions regarding the large wavelength at previous section. In this section, we would like to focus on the structure of the interfaces after rupture time when spinodal holes formed. We discuss the effect of thickness inhomogenouty on the location of first holes and it causing emergence of another wavelength.

Figure (4.21), demonstrates the time series of the evolution of PS-air interface on the same spot. The first spinodal hole forms after 22 min of annealing the sample (yellow circle on panel c) and as the number of holes increases, we observe clustering of the holes in some spots (panel e), creating repeated pattern of hills and gullies on a large scale that it amplifies with
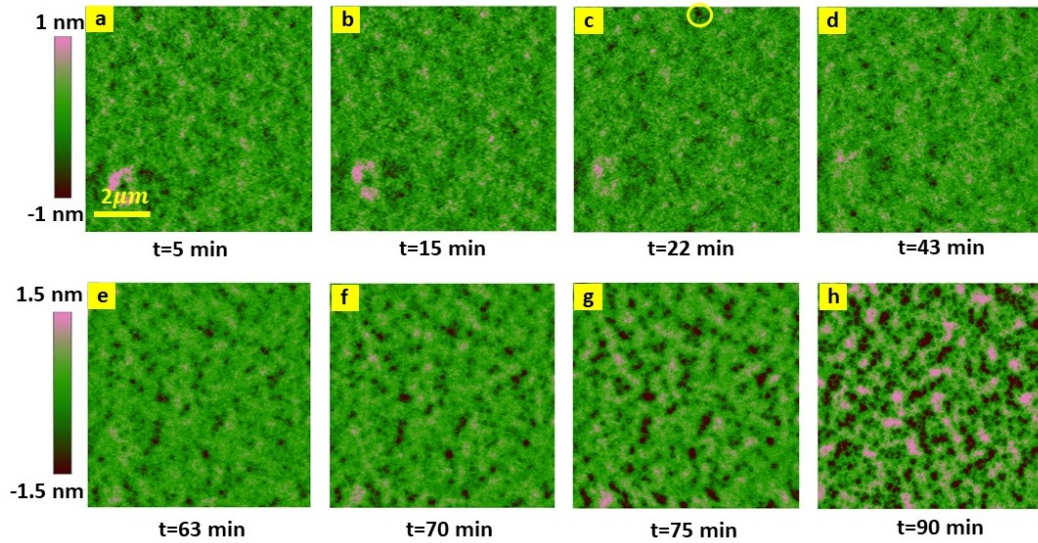
Figure 4.21: Topography of PS-air interface, captured in situ by AFM. A 7 nm of PS film on a 111 nm PMMA heated for 5 min (panel a), 15 min (panel b), 22 min (panel c), 43 min (panel d), 63 min (panel e), 70 min (panel f), 75 min (panel g) and 90 min (panel h) at $128°C$. The marked area on panel c, shows the location of the first spinodal hole.

time until spinodal holes form on other spots of the interface and they start to coalescence (panel h). We refer to this wavelength that forms after rupture time as secondary wavelength.

Although the formation and amplification of secondary wavelength is qualitatively visible from the images at figure (4.21), we applied power spectral density analysis to monitor that in more details, see figure (4.22). In the early stage of dewetting, before rupture, the detected wavelength is approximately 1300 nm on this particular sample that the location of peak is marked by red dashed line. This wavelength belongs to the waviness produced by preparation process (large wavelength). We notice a shift to a smaller wavelength in the range of 890 nm after rupture time (marked by black dashed line), indicating growth of a secondary wavelength that is the fastest growing wavelength in this stage of dewetting. The growth of secondary wavelength continues until other holes forms on all spots of the film where holes start to meet neighboring holes.

Figure (4.23) demonstrates the growth of the amplitude of the secondary wavelength as a function of heating time (red dots) that is extracted from the
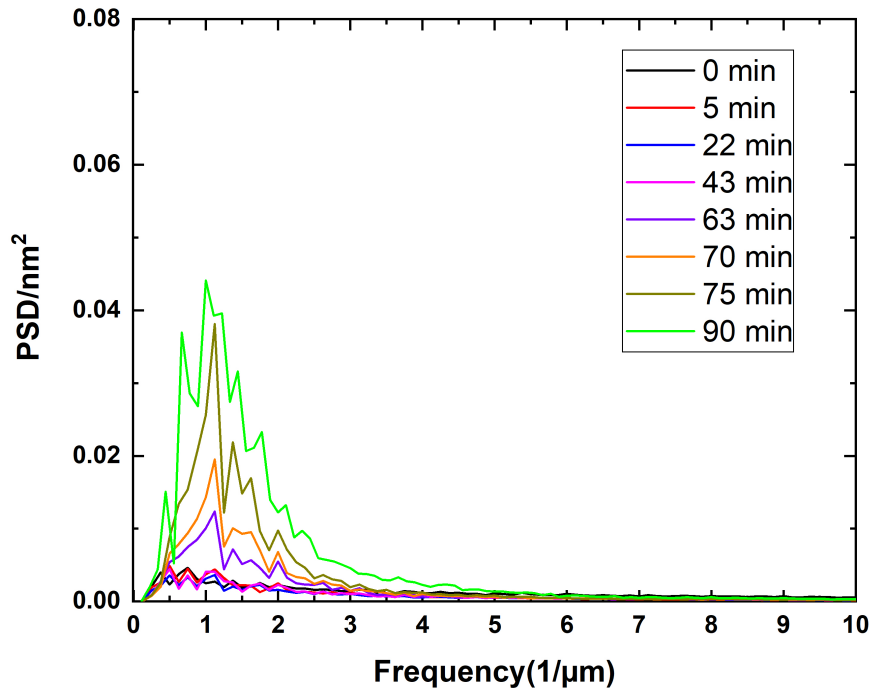
Figure 4.22: The time series of power spectral density analysis of the PS-air interface for different heating time. The sample with PS thickness of 7 nm on top of a PMMA layer of 111 nm heated at 128°C.

power of the power spectral density analysis. The blue dots on this graph are the amplitude of the large wavelength (waviness) that its signal disappears after rupture time.

The mechanism behind growth of the secondary wavelength is the thickness inhomogeneity of PS-air interface on mica and PMMA-air on silicone wafer after spin coating that is demonstrated at figure (4.2) at section (4.1). By conducting the dewetting experiment, the first holes form on the regions that initially have slightly lower thickness (valleys of the waviness) and the higher the thickness difference with other spots the longer the delay of the rupture time in spots and consequently the second holes also form on the valleys. Clustering of the holes on the valleys cause accumulation of more polymer material similar to the shape of a rim and with enlarging the holes the more polymer material is pushed away from center and is pilled up around. The accumulation of polymer
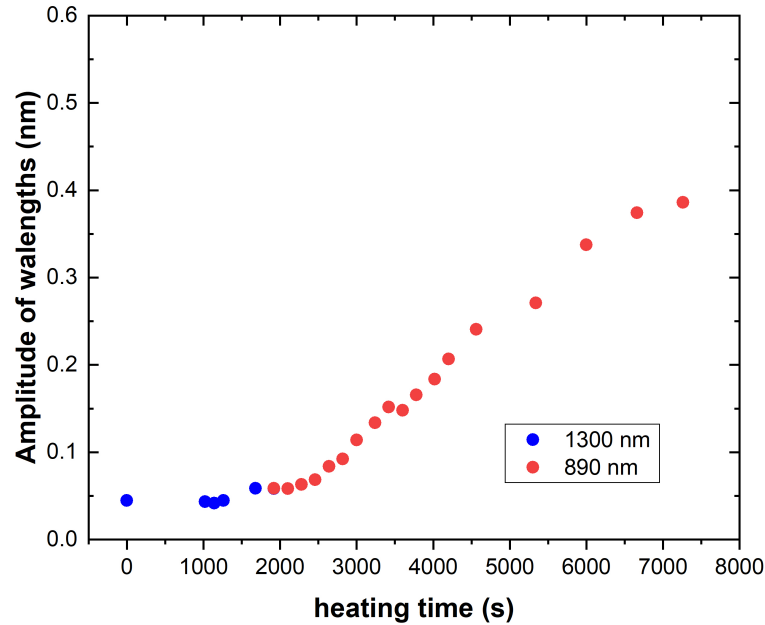
Figure 4.23: The dynamics of the large wavelength and the secondary wavelength on PS-air interface. The sample consist of a 7 nm PS film on top of a 111 nm PMMA annealed to the temperature of $128°C$.

material emphasizes the thickness inhomogeneity that causes the next holes to form on the valleys and as this process continues, the amplitude of secondary wavelength grows. Since the rupture time increase with the fifth power of the PS thickness (see figure 4.9), we expect the amplification of secondary wavelength to be more pronounced for thicker films and for thinner PS layer, the rupture time between the valleys and the hills decreases and it potentially could affect on the structure of interfaces in terms of the secondary wavelength.

Figure (4.24) compares the secondary wavelength for three different thickness of PS layer when the spinodal holes are well developed. As it is distinguishable the pattern regarding the secondary wavelength is less pronounced for smaller thicknesses due to shorter delay in the rupture time between the valleys and the hills of the wavinesses (panel a). For thicker PS layer that the PS film does not rupture due to spinodal dewetting the preferred holes distance does not exist, the secondary wavelength does not form (see figure 4.12).
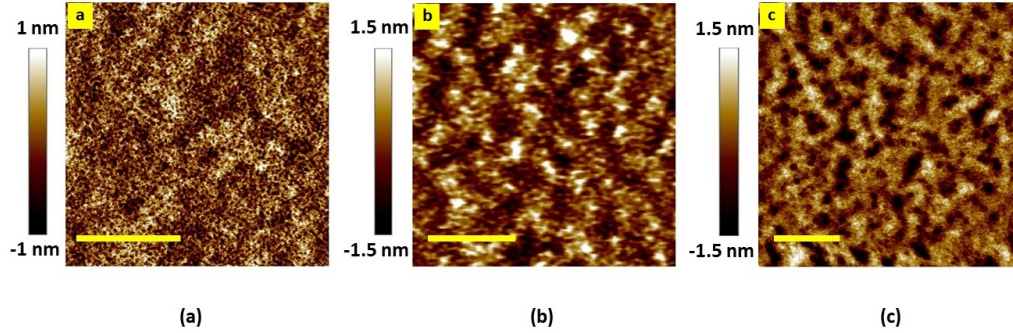
Figure 4.24: Topography of PS-air interface on PMMA layer of 111 nm, after rupture time. Panel a, PS layer with thickness of 5 nm, annealed for 32 min at 124°C, Panel b, PS layer with thickness of 6nm, annealed for 132 min at 124°C. Panel c, PS layer with thickness of 7nm, annealed for 74min 128°C. scale bar corresponds to $2\mu m$.

In conclusion, There are thickness inhomogeneity on both of the PS layer on mica sheet and PMMA layer on silicone wafer after spin coating. The structure on the PMMA is traced by thinner and smoother PS layer during transfer and two interfaces lock into each other creating the positive correlation of the waviness, although PS layer holds its thickness inhomogeneity and the holes form on the spots that have lower thicknesses. The growth of secondary wavelength is initiated by the thickness inhomogeneity and the delay in rupture time that corresponds to the thickness difference. Hence, in any other nucleation where a link for the rupture time as a function of thickness can not be found, it will not lead to the growth of secondary wavelength.

4.9 Equilibrium film thickness

As it is discussed at section (2.3), in our experimental system PS is unstable on PMMA and it dewets due to destabilizing Van der Waals forces and system minimizes its energy by reaching the global minimum of the effective interfacial potential that the depth of minimum is given by the spreading coefficient:

$$S_{eq} = \sigma_{PMMA-air}(\sigma_{PS-air} + \sigma_{PS-PMMA}) = -(0.7 \pm 0.1)\frac{mN}{m}$$

when using the surface tension values from ref. [50]. Using this minimum together with the long range part for the effective interface as given by the

Hamaker constant and assuming a short range part $\left(\frac{c}{h^8}\right)$ (section 2.3), we choose the value for the coefficient c in equation (2.6) until find the right value where the minimum of the curve is equal to the value of the spreading coefficient and thus the effective interface potential can be obtained, see figure (4.25).
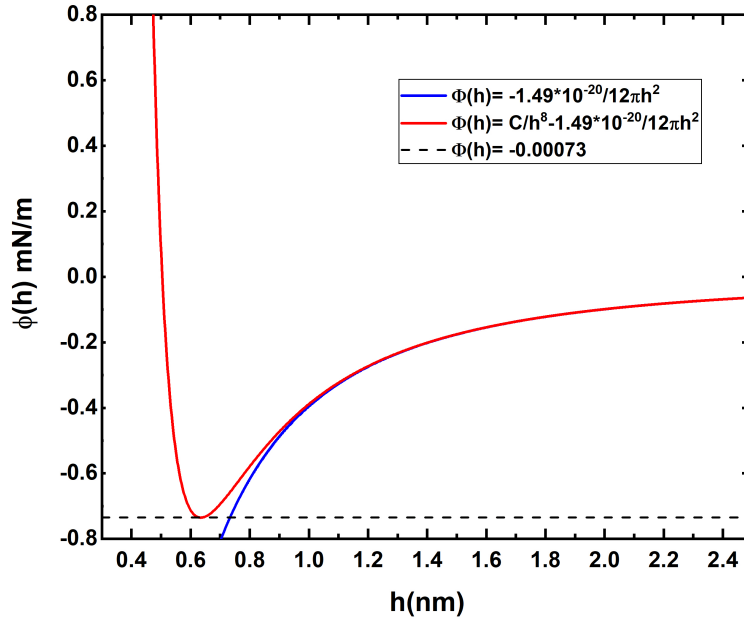

Figure 4.25: effective potential as a function of film thickness. The red line represents potential considering both of the long range and short range interactions, while the blue line includes only long range term.

According to the value of spreading coefficient, obtained by experiments and the potential model (equation 2.6), the equilibrium film thickness for our system extracted from figure (4.25) is around 0.6 nm. As this equilibrium film thickness is below the backbone diameter of a PS molecule it is interesting to check if there is an equilibrium film thickness that PS leaves behind after dewetting, then to measure the thickness and possibly compare it with the results from theory.

To confirm the existence of PS on PMMA, the peak force microscopy mode of the AFM gives promising results. This mode provides detailed information on material properties and enables us to distinguish different materials on the scanned area with more accuracy than the phase signal in tapping mode (3.1).

Therefore, if there is any PS left on the PMMA, the difference will be reflected in the adhesion property of materials.
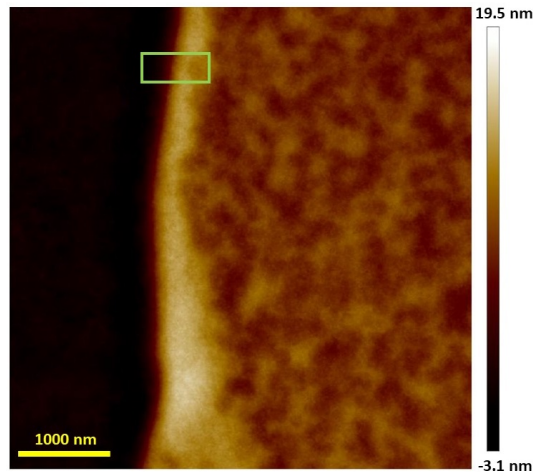

Figure 4.26: Dewetted PS film with thickness of 7 nm on top of a PMMA layer with thickness of 111 nm.

Figure (4.26) shows a random area on a sample that is partially covered with PS film on the right side of the image. The left side that is color coded with dark brown is covered only with PMMA substrate. The border between the two regions is called dewetting front (dewetting rim) that shows withdrawing PS film. The sample is heated to a temperature above T_g and as expected dewetted holes form on PS film that is captured as darker dots inside the PS film. To focus on one spot, we select a suitable spot (inside the box at figure (4.26), where includes three regions of bare PMMA, PS on top of PMMA and inside holes or dewetting front, see figure (4.27).
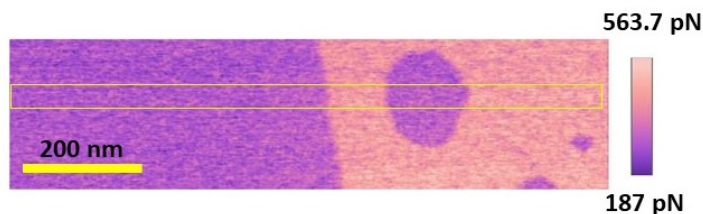
Figure 4.27: Adhesion map of the selected area on figure (4.26).

If PS completely dewets from PMMA substrate, the adhesivity of the region inside the holes must be identical to the adhesivity of the bare PMMA/air interface that is not covered with PS. Figure (4.27) qualitatively demonstrates the adhesivity of different regions on the sample. To compare the adhesion forces easier, we select a box that the final value of adhesion forces is an average over several scan lines inside that box and plot it as adhesion forces in the position of each pixel, see figure (4.28). The range between a-b is the bare PMMA/air interface that was not covered with PS. The range between b-c is the dewetting front and demonstrates the area from which the PS film has withdrawn (dewetted). The range between d-e demonstrates the region inside the hole. Comparing the value for the adhesion force for both of the area b-c and d-e that was covered with PS and has been dewetted, and comparing it with the rest of the area reveals that the adhesion forces on those spots are slightly larger than the adhesion forces on bare PMMA-air interface, meaning that there is some PS left.
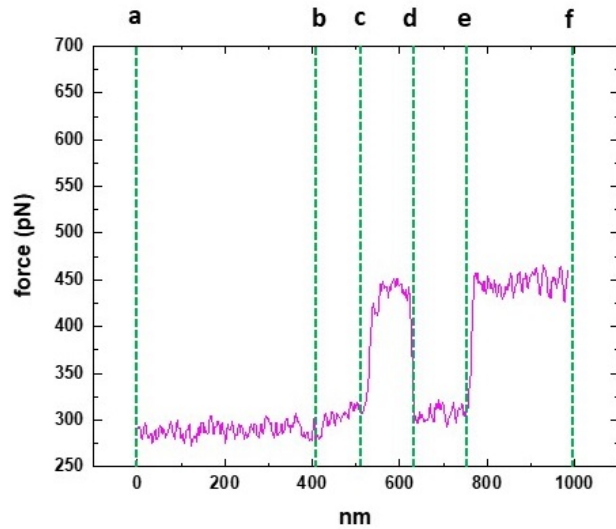
Figure 4.28: Average of adhesion force for the several scan line inside the box on figure (4.27).

To measure the thickness of the remaining PS layer on the substrate after dewetting, we apply ellipsometery measurement. In our experiments, polymers are prepared on silicone wafer and such a sample includes many interfaces and the reflected light from the surface in ellipsometery measurement is the combination of the light reflected from all the layers including silicone, silicone

dioxide, PMMA layer and the PS layer. Since the targeted PS layer for the measurement is expected to be very thin, the uncertainty from the thickness or refractive index of each of the material will influence on the thickness measurement of the PS film. How ever, precise measurement of the thickness of silicone dioxide and then PMMA layer after spin coating on top of that is one way to decrease the uncertainty. By conducting the dewetting experiment, the thickness of PMMA layer change due to flowing the polymers, and using the initial thickness of PMMA layer before dewetting experiments in the modeling, adds another uncertainty to the measurement of the thickness of remaining PS film on dewetted area. To avoid such issues, we used a thick glass of PMMA (1 cm) as the substrate and then by transferring PS film on top of that, we only deal with one layer. The refractive index of the glass is measured after
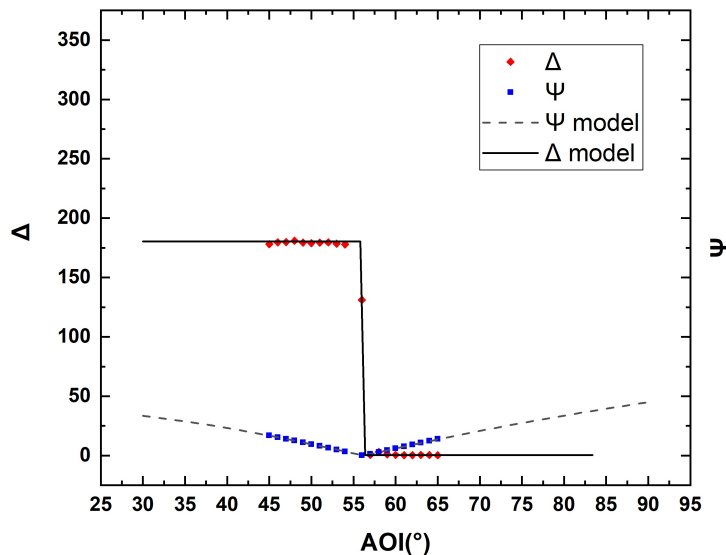
Figure 4.29: Ellipsometery measurement on PMMA glass with laser beam of 532 nm wavelength. The red diamonds demonstrate the measured data for Δ and blue squares are the measured data for (ψ) for different incident angle (AOI). The dashed line and the solid line are the data from modeling for (ψ) and Δ, respectively. The laser beam wavelength for the

annealing sample above the glass transition temperature for few hours, since the PMMA glass become more transparent after heating and consequently the refractive index might be different. Figure (4.29) demonstrates an ellipsometeric

measurement that is presented as the obtained (ψ) and (Δ) values and the analysis reveals the refractive index of the PMMA glass as 1.525.

To conduct the dewetting experiment, a PS film is transferred on top of the annealed PMMA glass and annealed them to $140°C$ inside an oven until dewetted holes formed. The thickness of PS in this measurement was chosen to be around 200 nm and since we analyze the data from inside the holes, the larger holes provides more pixels and consequently more data points. For that purpose, we used holes with around $200\mu m$ diameter.
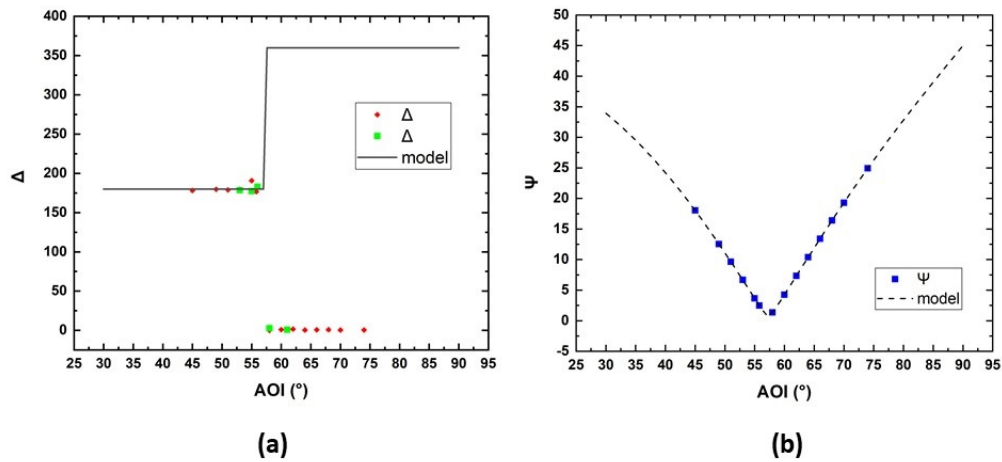
Figure 4.30: Ellipsometery measurement of PS residue on PMMA glass after dewetting. Panel a, shows the measured data (red diamonds and green square) for (Δ) from two different measurements and the data from modeling (solid line). Panel b, demonstrates the measured data (blue square) and modeling data (dashed line) for (ψ).

Figure (4.30) demonstrates the result of the measurement for the remaining PS film inside a dewetted hole. Comparing the result of PS thickness measurement with bare PMMA glass (figure 4.29) at the same angle of incident and same wavelength, shows slight variations on the (Δ) values around the Brewster angle indicating a surface with different properties with PMMA glass. However, the close value of refractive indices of PMMA glass (1.525) and PS (1.613) combined with the very small thickness of PS are causing difficulties in modeling of such system and consequently we could not been able to measure the PS thickness.

The adhesion forces measurement by AFM showed that the adhesion of the spots inside the holes are between the adhesion of the PMMA and PS. In

addition, the slight variation of the ellipsometery measurement of bare PMMA glass and inside the holes, suggest that the PS residue does not form a complete layer and there probably are only some molecules of PS left on the substrate after dewetting.

5

Summary and Outlook

This thesis aimed at explaining the dewetting path of a nano-metric thin liquid polymer (PS) from another liquid substrate (PMMA) with identical viscosity where the dewetting is driven by inter molecular Van der Waals forces. In this context, we found a preferred wavelength whose amplitude grows the fastest and eventually leads to the rupture of the upper PS film after a characteristic time. The preferred wavelength increases with thickness of the PS film and the rupture time scales with the fifth power of the PS thickness that is in accordance with theoretical predictions. We observed that for PS thickness above 8 nm, other hole nucleation processes lead to the rupture of PS film. The effect of thickness inhomogeneity on the location of first holes showed that they form on the spots that have slightly lower thickness. Since the rupture of PS film is due to the spinodal dewetting, the rupture time increases for spots with thicker PS film. Later on, with growth of the holes' rim, the thickness differences on the PS film is emphasized leading to the formation of a temporary peak on the power spectral density analysis.

The estimated equilibrium film thickness of PS on dewetted area based on effective interfacial potential model is lower than a complete monolayer of PS molecules. The result of peak force microscopy and ellipsometery measurements on the dewetted area, revealed that the PS residue did not form a complete layer and there are only some molecules of PS left on the substrate after dewetting.

The amplification of the spinodal wavelength was monitored by ex situ studies on PS-PMMA interface and it revealed the exponential growth of the spinodal corrugations. Comparing the deformation of PS-air and PS-PMMA interface on the same spot, short time before rupture, showed the negative correlation of spinodal corrugations that this observation is in agreement with theoretical predictions.

The deviation of the experimentally determined preferred wavelength with the results from theoretical prediction based on linear stability analysis revealed that the initial roughness and the initial correlation of the interfaces can surprisingly influence the mode selection process which is relevant only for liquid bilayers.

The dewetting of a liquid film from another liquid substrate is a general case that can be extended to two layer systems with different viscosity and thickness ratio and it remains to be seen if the theoretical predictions is right that different viscosity ratios mainly affect the characteristic break up time and the amplitude of each surface but hardly the wavelength. The similar experimental studies can be applied to non Newtonian regimes and to elastic substrates. However, the similar results obtained in this thesis is expected for a very soft substrates. Deviations are expected for elastic substrates that hinder the mobility of the elastic-viscous interface.

Bibliography

[1] JB Brzoska, N Shahidzadeh, and F Rondelez. Evidence of a transition temperature for the optimum deposition of grafted monolayer coatings. *Nature*, 360(6406):719–721, 1992.

[2] Pierre-Gilles De Gennes. Wetting: statics and dynamics. *Reviews of modern physics*, 57(3):827, 1985.

[3] Younan Xia, Enoch Kim, Xiao-Mei Zhao, John A Rogers, Mara Prentiss, and George M Whitesides. Complex optical surfaces formed by replica molding against elastomeric masters. *Science*, 273(5273):347–349, 1996.

[4] Henning Sirringhaus, Nir Tessler, and Richard H Friend. Integrated opto-electronic devices based on conjugated polymers. *Science*, 280(5370):1741–1744, 1998.

[5] Edwin WH Jager, Elisabeth Smela, and Olle Inganäs. Microfabricating conjugated polymer actuators. *Science*, 290(5496):1540–1545, 2000.

[6] Guenter Reiter. Dewetting as a probe of polymer mobility in thin films. *Macromolecules*, 27(11):3046–3052, 1994.

[7] G Krausch. Dewetting at the interface between two immiscible polymers. *Journal of Physics: Condensed Matter*, 9(37):7741, 1997.

[8] P Lambooy, KC Phelan, O Haugg, and G Krausch. Dewetting at the liquid-liquid interface. *Physical review letters*, 76(7):1110, 1996.

[9] Shichun Qu, CJ Clarke, Y Liu, MH Rafailovich, J Sokolov, KC Phelan, and G Krausch. Dewetting dynamics at a polymer- polymer interface. *Macromolecules*, 30(12):3640–3645, 1997.

[10] Ashutosh Sharma and Günter Reiter. Instability of thin polymer films on coated substrates: rupture, dewetting, and drop formation. *Journal of Colloid and Interface Science*, 178(2):383–399, 1996.

[11] R Xie, Alamgir Karim, Jack F Douglas, Charles C Han, and Robert A Weiss. Spinodal dewetting of thin polymer films. *Physical Review Letters*, 81(6):1251, 1998.

[12] A Vrij. Possible mechanism for the spontaneous rupture of thin, free liquid films. *Discussions of the Faraday Society*, 42:23–33, 1966.

[13] Von D Thiessen and A Scheludko. Dämpfung von zylindrischen stehenden kapillarwellen durch grenzflächenaktive stoffe. *Kolloid-Zeitschrift und Zeitschrift für Polymere*, 218(2):139–148, 1967.

[14] Eli Ruckenstein and Rakesh K Jain. Spontaneous rupture of thin liquid films. *Journal of the Chemical Society, Faraday Transactions 2: Molecular and Chemical Physics*, 70:132–147, 1974.

[15] LS Fisher and AA Golovin. Nonlinear stability analysis of a two-layer thin liquid film: Dewetting and autophobic behavior. *Journal of colloid and interface science*, 291(2):515–528, 2005.

[16] Andrey Pototsky, Michael Bestehorn, Domnic Merkt, and Uwe Thiele. Alternative pathways of dewetting for a thin liquid two-layer film. *Physical Review E*, 70(2):025201, 2004.

[17] Daniel Bonn, Jens Eggers, Joseph Indekeu, Jacques Meunier, and Etienne Rolley. Wetting and spreading. *Reviews of modern physics*, 81(2):739, 2009.

[18] M Gerovich, A Frumkin, and D Vargin. Dipole moment and surface potentials. *The Journal of Chemical Physics*, 6(12):906–906, 1938.

[19] Ralf Seemann, Stephan Herminghaus, Chiara Neto, Stefan Schlagowski, Daniel Podzimek, Renate Konrad, Hubert Mantz, and Karin Jacobs. Dynamics and structure formation in thin polymer melt films. *Journal of Physics: Condensed Matter*, 17(9):S267, 2005.

[20] F Brochard-Wyart and C Redon. Dynamics of liquid rim instabilities. *Langmuir*, 8(9):2324–2329, 1992.

[21] Karin Jacobs, Ralf Seemann, and Stephan Herminghaus. Stability and dewetting of thin liquid films. In *Polymer thin films*, pages 243–265. World Scientific, 2008.

[22] Ralf Seemann, Stephan Herminghaus, and Karin Jacobs. Gaining control of pattern formation of dewetting liquid films. *Journal of Physics: Condensed Matter*, 13(21):4925, 2001.

[23] Ralf Seemann, Stephan Herminghaus, and Karin Jacobs. Dewetting patterns and molecular forces: A reconciliation. *Physical Review Letters*, 86(24):5534, 2001.

[24] O Bäumchen, R Fetzer, and K Jacobs. Liquid front profiles affected by entanglement-induced slippage. *arXiv preprint arXiv:0907.2113*, 2009.

[25] Mihai Dorin Morariu. *Pattern formation by capillary instabilities in thin films.* University Library Groningen][Host], 2004.

[26] C Redon, F Brochard-Wyart, and F Rondelez. Dynamics of dewetting. *Physical review letters*, 66(6):715, 1991.

[27] Günter Reiter. Dewetting of thin polymer films. *Physical review letters*, 68(1):75, 1992.

[28] Jacob N Israelachvili. *Intermolecular and surface forces.* Academic press, 2011.

[29] William M Haynes. *CRC handbook of chemistry and physics.* CRC press, 2014.

[30] David R Lide et al. Handbook of chemistry and physics, 1998.

[31] John W Cahn. Phase separation by spinodal decomposition in isotropic systems. *The Journal of Chemical Physics*, 42(1):93–99, 1965.

[32] SBG O'brien and Leonard W Schwartz. Theory and modeling of thin film flows. *Encyclopedia of surface and colloid science*, 1:5283–5297, 2002.

[33] Stephan Harkema. *Capillary instabilities in thin polymer films*. PhD thesis, Ph. D. Thesis, University of Groningen, 2006.

[34] Sebastian Jachalski, Dirk Peschka, Andreas Münch, and Barbara Wagner. Impact of interfacial slip on the stability of liquid two-layer polymer films. *Journal of Engineering Mathematics*, 86(1):9–29, 2014.

[35] Bharat Bhushan. *Springer handbook of nanotechnology.* Springer, 2017.

[36] Daniel Ducharme, Alain Tessier, and Roger M Leblanc. Null ellipsometer for the studies of thin films at gas–water interface. *Review of scientific instruments*, 58(4):571–578, 1987.

[37] Brucker. *Manual of fast scan AFM.* Bruker Nano Surfaces and Metrology and the NanoScope Software User Guide, 2010.

[38] Leslie H Sperling. *Introduction to physical polymer science.* John Wiley & Sons, 2005.

[39] Thomas G Fox Jr and Paul J Flory. Second-order transition temperatures and related properties of polystyrene. i. influence of molecular weight. *Journal of Applied Physics*, 21(6):581–591, 1950.

[40] Stephan Herminghaus, Karin Jacobs, and Ralf Seemann. The glass transition of thin polymer films: some questions, and a possible answer. *The European Physical Journal E*, 5(1):531–538, 2001.

[41] David R Burfield. Polymer glass transition temperatures. *Journal of Chemical Education*, 64(10):875, 1987.

[42] Malcolm P Stevens. *Polymer chemistry*, volume 2. Oxford university press New York, 1990.

[43] Louis-Philippe Blanchard, Jean Hesse, and Shadi Lal Malhotra. Effect of molecular weight on glass transition by differential scanning calorimetry. *Canadian Journal of Chemistry*, 52(18):3170–3175, 1974.

[44] RB Beevers and EFT White. Physical properties of vinyl polymers. part 1.—dependence of the glass-transition temperature of polymethylmethacrylate on molecular weight. *Transactions of the Faraday Society*, 56:744–752, 1960.

[45] Fabio Zulli, Marco Giordano, and Laura Andreozzi. Chain-length dependence of relaxation and dynamics in poly (methyl methacrylate) from oligomers to polymers. *Macromolecules*, 51(5):1798–1810, 2018.

[46] Oliver Bäumchen, Renate Fetzer, Mischa Klos, Matthias Lessel, Ludovic Marquant, Hendrik Hähl, and Karin Jacobs. Slippage and nanorheology of thin liquid polymer films. *Journal of Physics: Condensed Matter*, 24(32):325102, 2012.

[47] Dirk Peschka, Stefan Bommer, Sebastian Jachalski, Ralf Seemann, and Barbara Wagner. Impact of energy dissipation on interface shapes and on rates for dewetting from liquid substrates. *Scientific reports*, 8(1):1–11, 2018.

[48] Oliver Bäumchen, Renate Fetzer, Mischa Klos, Matthias Lessel, Ludovic Marquant, Hendrik Hähl, and Karin Jacobs. Slippage and nanorheology of thin liquid polymer films. *Journal of Physics: Condensed Matter*, 24(32):325102, 2012.

[49] Ranxing N Li, Fei Chen, Chi-Hang Lam, and Ophelia KC Tsui. Viscosity of pmma on silica: Epitome of systems with strong polymer–substrate interactions. *Macromolecules*, 46(19):7889–7893, 2013.

[50] Stefan Bommer, Florian Cartellier, Sebastian Jachalski, Dirk Peschka, Ralf Seemann, and Barbara Wagner. Droplets on liquids and their journey into equilibrium. *The European Physical Journal E*, 36(8):1–10, 2013.

[51] FP Buff, RA Lovett, and FH Stillinger Jr. Interfacial density profile for fluids in the critical region. *Physical Review Letters*, 15(15):621, 1965.

[52] GH Gilmer, W Gilmore, J Huang, and WW Webb. Diffuse interface in a critical fluid mixture. *Physical Review Letters*, 14(13):491, 1965.

[53] SG Croll. The origin of residual internal stress in solvent-cast thermoplastic coatings. *Journal of Applied Polymer Science*, 23(3):847–858, 1979.

[54] Roghayeh Shiri, Ralf Seemann, Leonie Schmeller, Dirk Peschka, and Barbara Wagner. Spinodal dewetting of liquid-liquid thin films. *to be published.*

[55] MER Shanahan. The spreading dynamics of a liquid drop on a viscoelastic solid. *Journal of Physics D: Applied Physics*, 21(6):981, 1988.

Acknowledgements